RESEARCH ARTICLE

10.1029/2023WR034655

Key Points:

- Two pore-scale models for hydrodynamic flow and scalar transport and an inverse model for dispersion parameter estimation are developed
- Effects of spatial heterogeneity of porous media and flow nonlinearity on dispersive scalar transport are investigated
- Multi-scale analysis proposes the importance of the scale of the study to reliably capture the statistics of flow and scalar fields

Correspondence to:
M. Mousavi Nezhad,
m.mousavi-nezhad@warwick.ac.uk

Multi-Scale Analysis of Dispersive Scalar Transport Across Porous Media Under Globally Nonlinear Flow Conditions

Hamid Moghimi[1], Mohaddeseh Mousavi Nezhad[1] , and Alberto Guadagnini[2]

[1]Porous Materials and Processes Modelling Research Group, Warwick Centre for Predictive Modelling, School of Engineering, The University of Warwick, Coventry, UK, [2]Dipartimento di Ingegneria Civile e Ambientale, Politecnico di Milano, Milano, Italy

Abstract We focus on nonlinear flow regime scenarios observed at the global scale of a porous medium and explore the impact of such nonlinearities on key features of dispersive scalar transport observed across three-dimensional porous systems characterized by various degrees of pore space complexity. Flow and transport processes are analyzed at pore-scale and larger scales in well-documented digital Beadpack and Bentheimer sandstone samples. Our simulations comprise linear (Darcy) and nonlinear (Forchheimer) flow regimes and consider a broad interval of values of Péclet number (ranging from 1×10^{-2}–5×10^4). Sample probability density functions of pore-scale velocities and concentrations of the migrating scalar are analyzed and related to flow conditions and degree of complexity of the pore space. Estimated values of dispersion associated with section-averaged breakthrough curves display a power-law scaling on the Péclet number. The scaling exponent depends on the relative importance of pore-scale diffusion and advection. We find that the Forchheimer flow regime is characterized by enhanced mixing of the scalar field. This leads to enhanced dispersion as compared against a Darcy regime.

1. Introduction

The need for enhanced assessment of key features of nonlinear flow conditions manifesting across a porous medium and their influence on dispersive scalar transport taking place therein is associated with significant applications in various industrial, biological, and environmental applications. These include groundwater and soil protection against contamination, agriculture, chemical mixing and reactions, subsurface energy development and storage, or water filtration across variably saturated systems.

Experimental and numerical studies have been focused on the characterization of hydrodynamic flow patterns and scalar dispersion in porous media using various approaches (e.g., Dong et al., 2022; Mousavi Nezhad & Javadi, 2011). Investigations have been conducted to assess the effects of quantities such as, for example, the range of pore-scale velocities and the structural complexity of the pore space on dispersive features emerging at the overall scale of the system in association with the transport of passive scalars (Zhang et al., 2021 and references therein). Experimental investigations of hydrodynamic processes and scalar dispersion in porous media typically rely on column tests. As a recent example, Van Offenwert et al. (2019) illustrate an experimental study focused on the feedback between scalar spreading and mixing and spatial heterogeneity of pore structure. Their results document a direct relationship between pore space heterogeneity and parameters controlling hydrodynamic dispersion at the Darcy-scale. Mousavi Nezhad et al. (2019) assess scalar dispersion across porous media associated with differing characteristic sizes of particles forming the solid matrix under globally nonlinear flow conditions. In a related study, Gaiselmann et al. (2014) explore the impact of the microstructure of porous media on transport processes taking place therein. In their study, the Authors employ a set of Monte Carlo replicates of the pore space to analyze the impact of the porous structure on transport phenomena. This is framed in the context of an analysis according to which the flow characteristics of the porous domain, such as conductivity and porosity, are viewed as random fields. Their findings indicated a significant effect of microstructure on transport processes, thus highlighting the importance of considering such factors in the characterization and modeling of flow and transport across porous media.

Direct numerical simulations (DNS) are employed to illustrate pore-scale flow patterns and scalar dispersion (e.g., Blunt et al., 2013; Zahasky & Benson, 2022 and references therein). These studies usually rest on high-resolution three-dimensional pore structures provided by X-ray CT imaging (see, e.g., Mostaghimi et al., 2013; Van Offenwert et al., 2021 and references therein, amongst others) within which relevant processes

Project Administration: Mohaddeseh Mousavi Nezhad
Resources: Mohaddeseh Mousavi Nezhad
Supervision: Mohaddeseh Mousavi Nezhad, Alberto Guadagnini
Validation: Hamid Moghimi
Visualization: Hamid Moghimi, Mohaddeseh Mousavi Nezhad
Writing – review & editing: Hamid Moghimi, Mohaddeseh Mousavi Nezhad, Alberto Guadagnini

can be simulated numerically. Typical pore-scale modeling studies are based on finite volume approaches (FVM; e.g., Moghimi et al., 2022; Mostaghimi et al., 2013) and/or the Lattice-Boltzmann method (LBM; e.g., Poureslami et al., 2021; Vasheghani Farahani et al., 2020). Results depict slower and more complex transport features across porous media with an increased degree of pore structure heterogeneity. Geostatistical approaches have also been used to quantify effective transport parameters associated with porous domains with heterogenous pore structures and complex pore-scale flow fields (e.g., Aramideh et al., 2018; Zhang et al., 2019). With reference to nonlinear flow regime scenarios observed at the global scale of the system under investigation, it has been empirically concluded that the dispersion parameter increases nonlinearly with the Péclet number (Delgado, 2007). Several empirical formulations have been proposed to quantify such a dependence. Their ability to capture the observed behavior varies depending on the flow regime (Icardi et al., 2014), and it has been shown that their robustness is highest for low Péclet numbers in heterogeneous porous media (Sadeghi et al., 2020). Inverse modeling studies have also been performed to estimate the value of macro-dispersion coefficients from pore-scale data in porous media subject to steady-state single- and two-phase flow in the Darcy regime (Aziz et al., 2018; Metcalfe et al., 2022 and references therein). Otherwise, analyses considering nonlinear flow regimes are still scarce. A theoretical framework based on an upscaled Continuous Time Random Walk (CTRW) is also used to interpret transport behaviors observed at the macro-scale (Talon et al., 2023).

Several efforts have been made to quantify macro-dispersion in porous media with various degrees of complexity. However, the connection between flow nonlinearity observed at the macro scale, spatial heterogeneity of the pore space, and the spread of scalar quantities in the system is still not completely explored. Most previous studies focused on pore-scale analyses of porous domains within which a (nonlinear) Forchheimer regime takes place are typically aimed at characterizing macro-scale (or effective) parameters only at high Péclet numbers (Wang, 2021; Zhou et al., 2019). Moreover, a robust assessment of the impacts of spatial heterogeneities of pore spaces on scalar dispersion and on spatial variability of flow under nonlinear flow settings is still only partly documented (Thakur et al., 2022).

As such, our study is keyed to the assessment of the effects of (macro-scale) flow nonlinearity on dispersive scalar transport across three-dimensional porous systems of various degrees of spatial heterogeneity (in terms of their pore structure). We rely on direct pore-scale studies and consider a wide range of values of the Péclet number. We analyze the behavior of flow and transport processes at the pore-scale and at larger scales encompassing (a) section-averaged (i.e., one-dimensional) representations of transport and (b) the whole porous domains under investigation. Well-documented images of a Beadpack and a Bentheimer sandstone samples are employed in our multi-scale analyses. Effective dispersion parameters are evaluated (together with their associated estimation uncertainty) through an inverse modeling framework based on a classical Maximum Likelihood Method.

2. Materials and Methods

Pore-scale analyses of fluid flow and scalar transport are performed on three-dimensional porous media reconstructed from a detailed close-packing approach and X-ray CT images. We rely on direct simulations of the Navier-Stokes and Advection-Diffusion equations, driving pore-scale fluid flow and transport of a given scalar, respectively. The flow scenarios analyzed are designed to correspond to linear and nonlinear flow regimes at the overall scale of the porous domain. We rely on these detailed simulations to explore distributions and patterns of pore-scale velocities and scalar concentration fields across these two flow regimes and for a vast array of values of a characteristic Péclet number associated with the system. We also (a) interpret the ensuing (section-averaged) breakthrough curves (BTCs) of the scalar field through a (macroscopic) one-dimensional formulation of the Advection-Dispersion equation and (b) assess the estimate (and its associated uncertainty) of the associated hydrodynamic dispersion parameter through inverse modeling framed in the context of Maximum Likelihood. Details of the approach are described in the following.

2.1. Pore-Scale Geometry

The three-dimensional pore spaces we analyze are grounded on well-established images of a Beadpack sample and a Bentheimer sandstone. The Beadpack sample image is generated by using a random close-packing approach to measure the coordinates of the centers of spherical grains with the same size (Prodanović & Bryant, 2006). Also, the pore-space image of Bentheimer sandstone is generated by X-ray CT imaging approach (Muljadi et al., 2016).
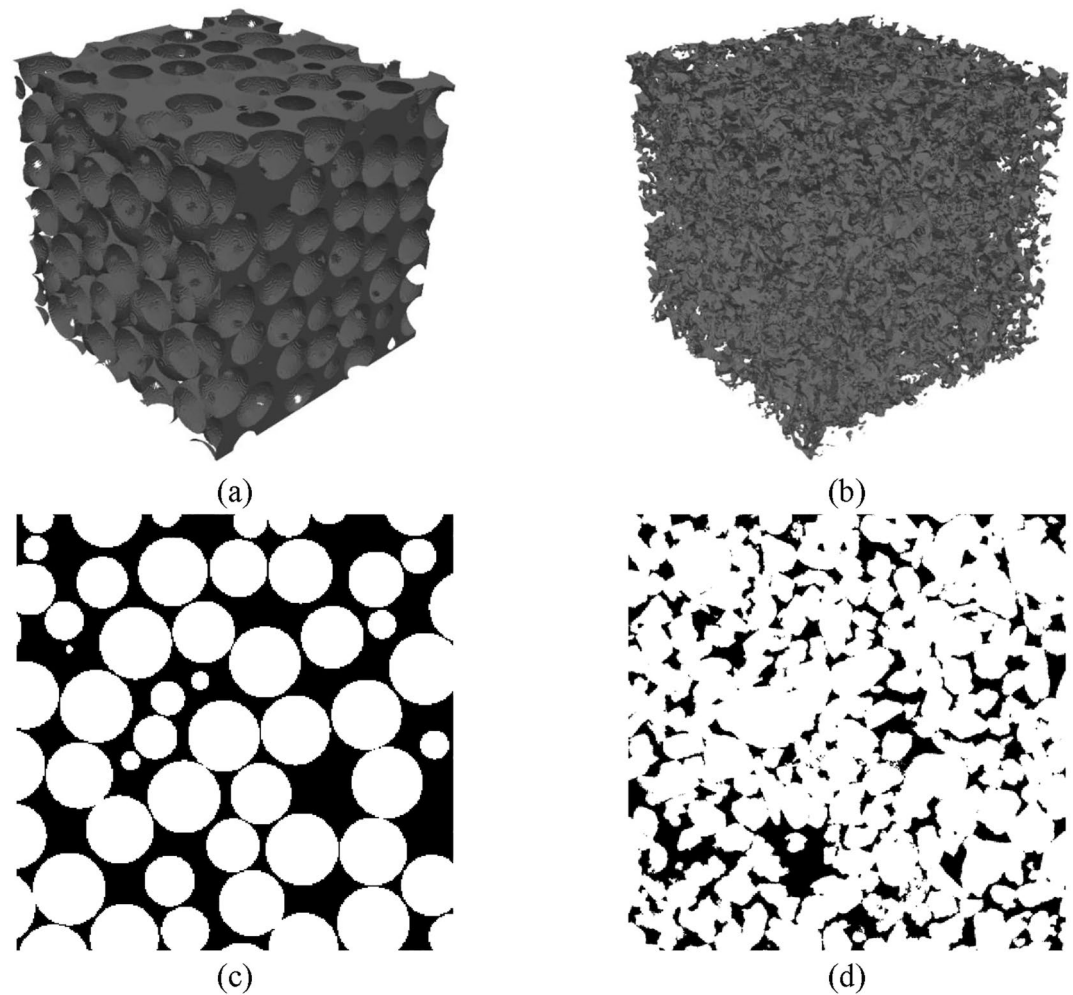
Figure 1. Three-dimensional pore spaces associated with (a) Beadpack sample and (b) Bentheimer sandstone, obtained through X-ray CT imaging (Muljadi et al., 2016) and random close-packing approach (Prodanović & Bryant, 2006), respectively; and selected two-dimensional (2D) cross-sections of (c) Beadpack and (d) Bentheimer structures.

Figures 1a and 1b depict the ensuing three-dimensional porous structures. As one can note, these are character-ized by notably differing degrees of complexity. Figures 1c and 1d complement the depiction, offering selected two-dimensional cross-sections of these structures. Table 1 lists the main characteristics of the images of the two porous samples, including the overall sample size, porosity, and characteristic length (L), representing the mean pore diameter of the porous structure (see also El-Zehairy et al., 2019).

The choice of porous domains for both samples is informed by the findings of El-Zehairy et al. (2019) and Muljadi et al. (2016). We further note that our analyses are associated with various spatial windows of investiga-tion. Each of these is treated as a well-defined observation scale which is considered as a continuum. Similar to Guadagnini and Neuman (2001), we only require that such a scale corresponds to a volume at which quantities of interest can be (in principle) assessed, either directly or indirectly. Thus, the spatial/temporal scales considered in our analysis enable one to address the effects of local heterogeneities. The latter are not necessarily related to

Table 1
Main Characteristics of the X-Ray CT Images of the Porous Samples Considered

Sample	Resolution (μm)	Pore voxels	Sample cube dimensions (mm)	L (μm)	Porosity
Beadpack	2	$300 \times 300 \times 300$	0.6	100.0	0.359
Bentheimer	3	$500 \times 500 \times 500$	1.5	139.9	0.211

the concept a representative elementary volume (REV). This view is also consistent with the general elements underpinning classical stochastic approaches targeting randomly heterogeneous porous media and process taking place therein.

The mesh employed in our numerical simulations of pore-scale and transport comprises hexahedral cells. It is generated through the broadly used and well-tested SnappyHexMesh utility available on the OpenFOAM platform (Jasak et al., 2007). Details of the mesh generation methodology are illustrated in the supporting information together with an analysis on the influence of grid-spacing on numerical results.

2.2. Governing Equations

Pore-scale steady-state incompressible fluid flow across a rigid porous medium is described through mass conservation and upon relying on the direct numerical simulation (DNS) of the Navier-Stokes equations, that is,

$$\nabla . \boldsymbol{u}_p = 0 \tag{1}$$

$$(\boldsymbol{u}_p . \nabla)\boldsymbol{u}_p = -\frac{1}{\rho} \times \nabla p + \vartheta \nabla^2 \boldsymbol{u}_p + \boldsymbol{g} \tag{2}$$

where, p and $\boldsymbol{u}_p$ represent fluid pressure and velocity vector across the pore space, respectively; ρ and ϑ denote (constant) fluid density and kinematic viscosity, respectively; and $\boldsymbol{g}$ represents gravity.

When considering the overall scale of the porous systems, we describe the (generally nonlinear) flow through the porous domain by

$$-\nabla p = \frac{\mu}{\boldsymbol{k}_D}\boldsymbol{U} + \rho\beta U^2\boldsymbol{n} \tag{3}$$

where, β is the Forchheimer coefficient; ∇p represents the pressure gradient across the system; $\boldsymbol{U}$ is the Darcy velocity vector (U being its norm); $\boldsymbol{k}_D$ and μ are the intrinsic permeability tensor of the porous system and dynamic viscosity of the fluid, respectively; and $\boldsymbol{n}$ is a unit vector aligned with ∇p. Equation 3 reduces to Darcy's law when $\beta = 0$. Such a scenario corresponds to (continuum-scale) flow through porous media at low Reynolds numbers (i.e., corresponding to a linear regime where inertia effects are negligible). An overall nonlinear flow behavior is typically documented as the Reynolds number increases and inertial effects begin to emerge. We rely on the following formulation for the Reynolds number in our analyses, that is,

$$\text{Re}_l = \frac{\rho U L_{\text{charc}}}{\mu} \tag{4}$$

where, L_{charc} is a characteristic length scale. Following Huang et al. (2019), we take the latter to correspond to the mean pore diameter of the porous system (denoted as L in Table 1).

The numerical solution of the pore-scale velocity field is then employed to analyze passive scalar migration and the associated spreading across the considered porous spaces. Solute transport analysis rests on the numerical solution of the Advection-Diffusion equation
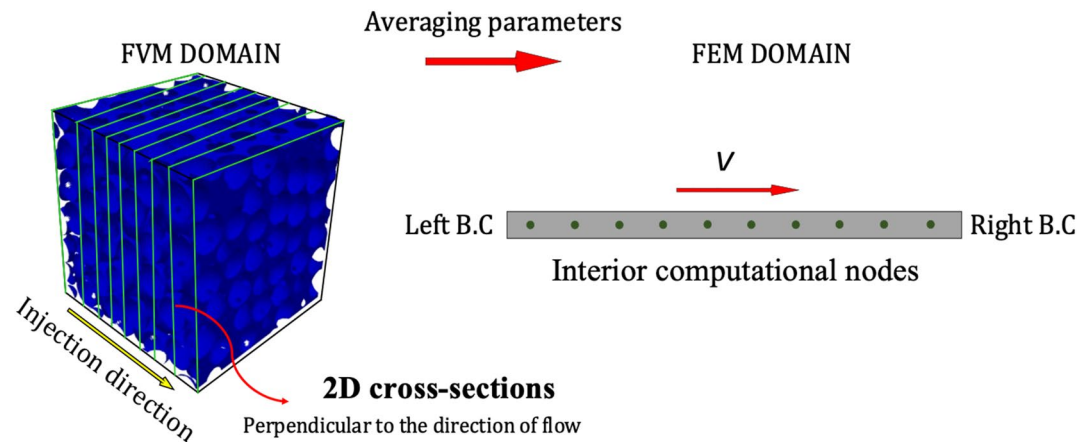
$$\frac{\partial c}{\partial t} + \nabla . (\boldsymbol{u}_p c) - D_m \nabla^2 c = 0 \tag{5}$$

where, c and $\boldsymbol{u}_p$ are the pore-scale solute concentration and velocity vector, respectively; t is time; and D_m is the (constant) molecular diffusion coefficient.

Macro-scale solute dispersion is characterized through the following (one-dimensional) formulation embedding section-averaged quantities

$$\frac{\partial C}{\partial t} = -V\frac{\partial C}{\partial x} + D\frac{\partial^2 C}{\partial x^2} \tag{6}$$

Note that

Figure 2. Schematic view of the relationship between three-dimensional and section-averaged system representations.

$$V = \frac{\int_0^{L_y} \int_0^{L_Z} v_x \, dy \, dz}{\epsilon(x) \, L_y L_Z} \tag{7}$$

where V is the average of the magnitude of pore velocity (at each cross-section); and $\epsilon(x)$ is porosity associated with the given cross section; v_x is the magnitude of pore velocity in flow direction; and L_y and L_z are the sample dimensions along directions y and z, respectively. The macro-scale hydrodynamic dispersion coefficient (D) includes the contribution of (a) molecular diffusion and (b) dispersion. Dispersive scalar transport is analyzed considering various values of the Péclet number, defined as (e.g., Bijeljic et al., 2004)

$$\text{Pe} = \frac{V \, L_{\text{charc}}}{D_m} \tag{8}$$

2.3. Workflow and Numerical Implementation

The open-source CFD platform OpenFOAM (Jasak et al., 2007) is used to perform pore-scale simulations of flow and transport across the pore spaces illustrated in Section 2.2. Incompressible steady-state fluid flow is simulated upon relying on the NonDarcyFoam solver, which solves the governing flow equations through a widely used semi-implicit method for pressure-linked equations (SIMPLE). The developed solver uses an implicit, second-order upwind divergence scheme for the discretization of the Navier-Stokes equations. Convergence conditions for the numerical simulations are defined upon setting absolute differences between model outputs (i.e., pressure and velocity at each point in the domain) obtained at two subsequent iterations to be less than 1×10^{-6} Pa and 1×10^{-7} m/s for pressure and velocity magnitude, respectively. The evaluated velocity field is then used as input to the scalar transport solver SoluteTransportFoam to solve Equation 5. All terms of the governing formulations are discretized implicitly, using the FVM family of operators. The solver "SoluteTransportFoam" is based on the OpenFOAM platform (Jasak et al., 2007). The latter employs a finite volume method to numerically solve the advection-diffusion equation. The advection term is solved through a first-order upwind scheme, solution of the diffusion term relying on a second-order central difference scheme. Here, the solver is employed to simulate scalar transport through complex heterogeneous porous domains under non-linear flow conditions.

We obtain an estimate, D^*, of the (macro-scale) dispersion coefficient D in Equation 6 within a classical Maximum Likelihood model calibration framework. In this context, model parameter estimation is performed upon conditioning Equation 6 on (section-averaged) breakthrough curves (BTC) obtained from the pore-scale flow and transport simulations. As illustrated in Figure 2, solute BTCs are evaluated at a collection of cross-sections normal to the main flow direction.

Figure 3 depicts the workflow designed for the study. Pore-scale velocity and scalar concentrations are evaluated across the computational domains as described in Section 2.2. The average velocity to be used as input to
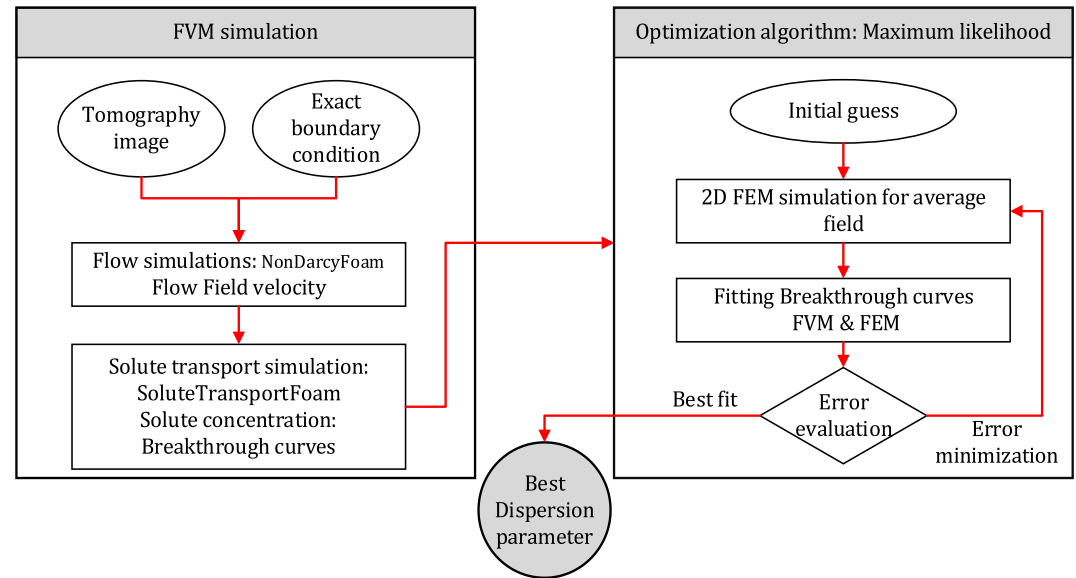
Figure 3. Overview of the workflow employed in the present analyses.

Equation 6 is evaluated according to Equation 7. Section-averaged concentrations for each time step (i.e., corresponding to BTCs) are evaluated as

$$C(x,t) = \frac{\int_0^{L_y} \int_0^{L_Z} c_p \, dy \, dz}{\epsilon(x) \, L_y L_Z} \tag{9}$$

where, $C(x,t)$ is section-averaged concentration (see also Equation 6; and $c_p(y,z,t)$) is pore-scale concentration.

Statistical analyses aimed at evaluating sample variogram and probability density function (PDF) of pore velocities and scalar fields are performed upon relying on the widely known and tested toolbox GSTools (version 1.3.5; Müller et al., 2021). The latter is a comprehensive open-source toolbox for geostatistical modeling and statistical data analysis that is designed according to a modern object-oriented approach. Using this toolbox, we estimate values of D^* as well as their associated uncertainty (expressed through the ensuing estimation variance) via classical Maximum Likelihood.

The main goal of this study is to offer an accurate description of flow and scalar transport across heterogeneous pore spaces and provide a detailed analysis of the main features emerging at various observation scales in the presence of linear and nonlinear flow regimes. The assessment of the ability and relative merits of upscaled transport models (including, e.g., upscaled CTRW or multi-rate mass transfer models) to interpret section-averaged transport features will be the subject of future studies.

3. Numerical Results and Analysis

3.1. Problem Setting

We investigate the importance of pore-scale flow features on scalar transport across a wide range of Péclet number values (i.e., spanning across the range 1×10^{-2}–5×10^4). Figure 4 depicts the key elements associated with the boundary conditions employed in the numerical pore-scale simulations. A wide range of values of (constant) pressure gradients (1×10^{-5}–30 MPa/m) between the inlet and outlet cross-sections of the porous structure is considered to model fluid flow in the x-direction, this enables us to obtain various values of Pe. A continuous uniformly distributed solute source is applied at the inlet boundary. A free-flow boundary condition is applied at the outlet of the domain. All solid walls of the porous domain are considered as impermeable. The diffusion coefficient employed in Equation 5 is set to $D_m = 1 \times 10^{-9}$ m²/s.
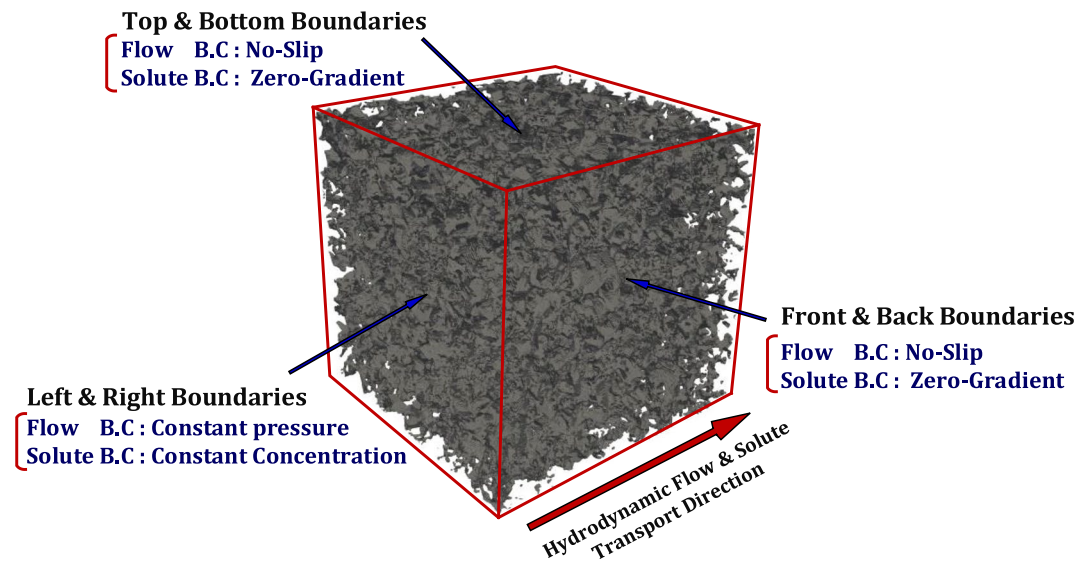
Figure 4. Main elements associated with the boundary conditions employed in the numerical pore-scale flow and transport simulations across the Beadpack and Bentheimer sandstone samples.

The analysis encompasses two distinct scales. These correspond to the pore- and the Darcy- (or macro-) scale, respectively. Our analyses at the pore-scale include the assessment of the flow field within individual pores of the porous structures considered. The characteristic length scale associated with these investigations corresponds to 100 and 139.9 μm for the Beadpack sample and Bentheimer Sandstone, respectively. Darcy-scale refers to viewing porous media as a continuous system with average properties. Flow at this scale is considered to be governed by Darcy's or Forchheimer's laws. These relate flow rate to pressure gradient across the porous medium, allowing for the assessment of an overall flow behavior. To appraise macro-scale behavior, one defines porous domain attributes such as permeability, porosity, and dispersion upon examining the average behavior of flow and scalar fields. At the Darcy-scale, physical length is represented by the characteristic length of the sample cubes, which is 0.6 mm for the Beadpack sample and 1.5 mm for Bentheimer sandstone.

3.2. Dispersive Scalar Transport

The quality of the numerical framework for hydrodynamic flow simulations has been successfully assessed against previous results obtained from pore-scale simulation methods, including finite volume (Muljadi et al., 2016) and pore network modeling approaches (El-Zehairy et al., 2019). A multi-scale analysis similar to the one illustrated by Moghimi et al. (2022) is considered to evaluate the permeability of the heterogeneous porous samples. This yields permeability values of 5.54×10^{-12} and 3.38×10^{-12} m² for the Beadpack and Bentheimer samples, respectively. We note that flow taking place across the Bentheimer sandstone domain enters the (nonlinear) Forchheimer regime at a value of the Reynolds number $Re_l = 0.184$. The latter is lower than the corresponding value (i.e., $Re_l = 2.63$) documented for the Beadpack sample. This finding is related to the different degrees of pore space heterogeneity associated with the two pore spaces.

Figure 5 depicts some exemplary (three-dimensional) temporal snapshots of concentration distributions within the Beadpack and the Bentheimer sandstone samples for a setting associated with the Forchheimer regime. Visual inspection of the results reveals that, due to the complex geometry of the heterogeneous pore structures, preferential flow paths (i.e., corresponding to the wide pores that carry high volumes of the migrating scalar) are visible. These, in turn, underpin the occurrence of fingered-like solute spreading patterns driving local concentration gradients, as we can also see in the following.

Estimates of the (macro-scale) dispersion coefficient and their associated (estimation) uncertainty (as rendered through estimation variance) are obtained through Maximum Likelihood at 25 values of the Péclet number spanning, as stated above, Darcy and Forchheimer regimes. The ensuing (normalized) results are depicted in Figure 6 versus Pe. This also enables us to compare our estimates with values obtained through previous
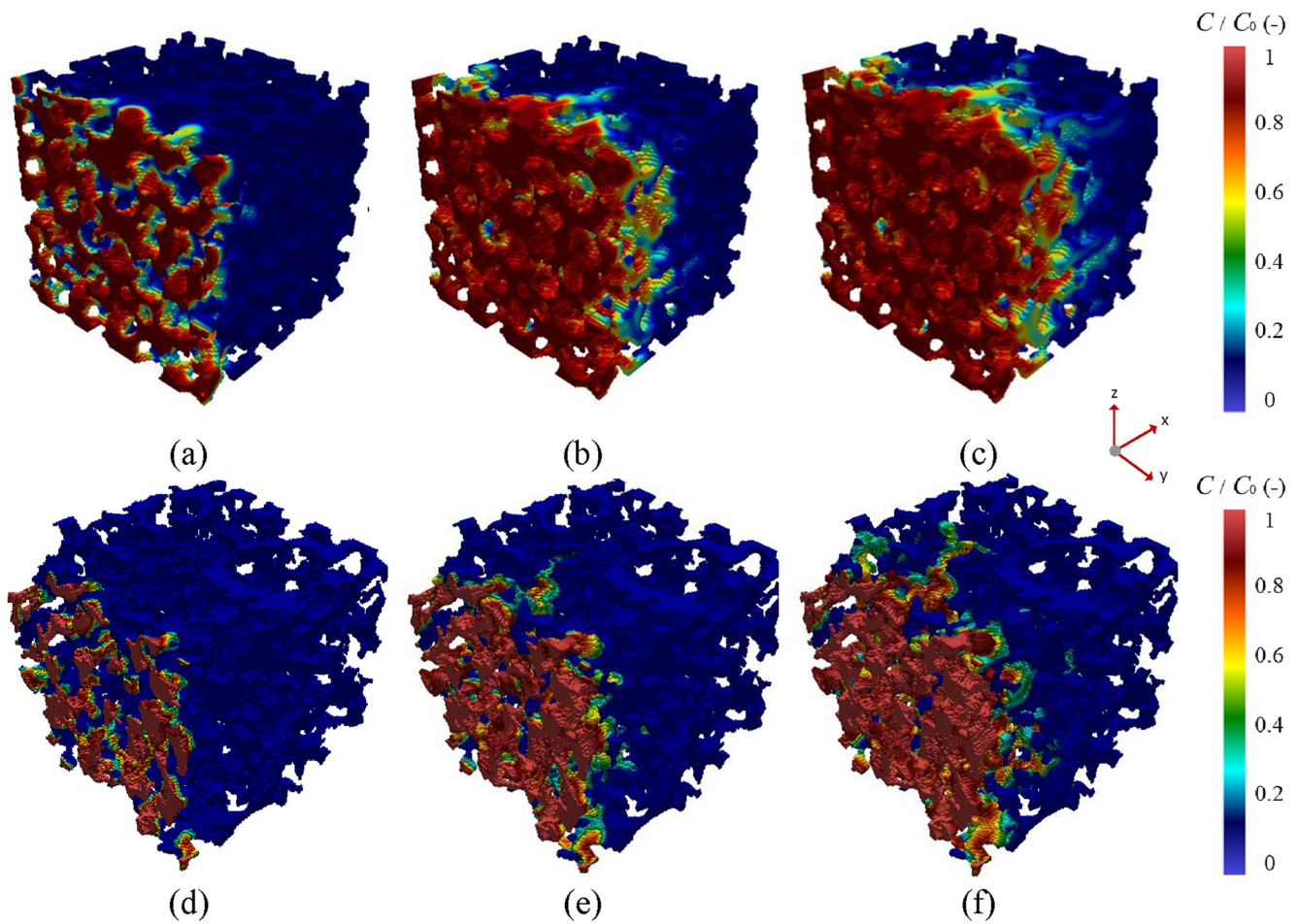
Figure 5. Exemplary three-dimensional snapshots of concentration distributions within the Beadpack and the Bentheimer sandstone samples for a setting associated with the Forchheimer regime and Pe = 10,000. Observation times correspond to (a) 0.001 s, (b) 0.005 s, (c) 0.01 s for the Beadpack sample and (d) 0.001 s, (e) 0.003 s, and (f) 0.006 s for the Bentheimer sandstone domain.

numerical (Bijeljic et al., 2004) and experimental (Khrapitchev & Callaghan, 2003; Pfannkuch, 1962; Seymour & Callaghan, 1997; Stöhr, 2003) analyses performed for Beadpacks. It can be noted that molecular diffusion is the dominant mechanism controlling transport behavior at low Péclet numbers (Pe < 1), where the contribution of the advection mechanism is negligible. The solid phase acts as a barrier and typically contributes to reduce the effective diffusion of the scalar. Such a reduction of diffusion is clearly seen in the low Péclet number region, where $D/D_m < 1$. By increasing the Péclet number (corresponding to a scenario where flow enters the transition regime where the contribution of the advection mechanism is enhanced), dispersive transport is governed by both diffusion and mechanical dispersion, the latter being related to spatial heterogeneities of the pore-scale velocity field. Impacts of advection are more prominent at higher Péclet numbers (i.e., 10 < Pe < 100. In these settings, the scalar migrates with higher velocity through the pores with larger throats. The advection mechanism is dominant at values of the Péclet number where flow is associated with an (overall nonlinear) Forchheimer regime (i.e., Pe > 500). This causes the fast advancement of the scalar through the central zone of the larger pores, forming, in turn, several local zones with high concentration gradients. This is clearly evidenced through the contour plots depicted in Figures 7 and 8. The importance of dispersion increases up to 5 orders of magnitude, as compared against diffusion (i.e., $D \approx D_m \times 10^5$), evidencing the influence of inertial flow on solute dispersion.

The estimated dispersion values are seen to increase according to a power-law behavior for both porous media samples. Our results could then be interpreted through the following set of relationships, depending on the range of values for Pe
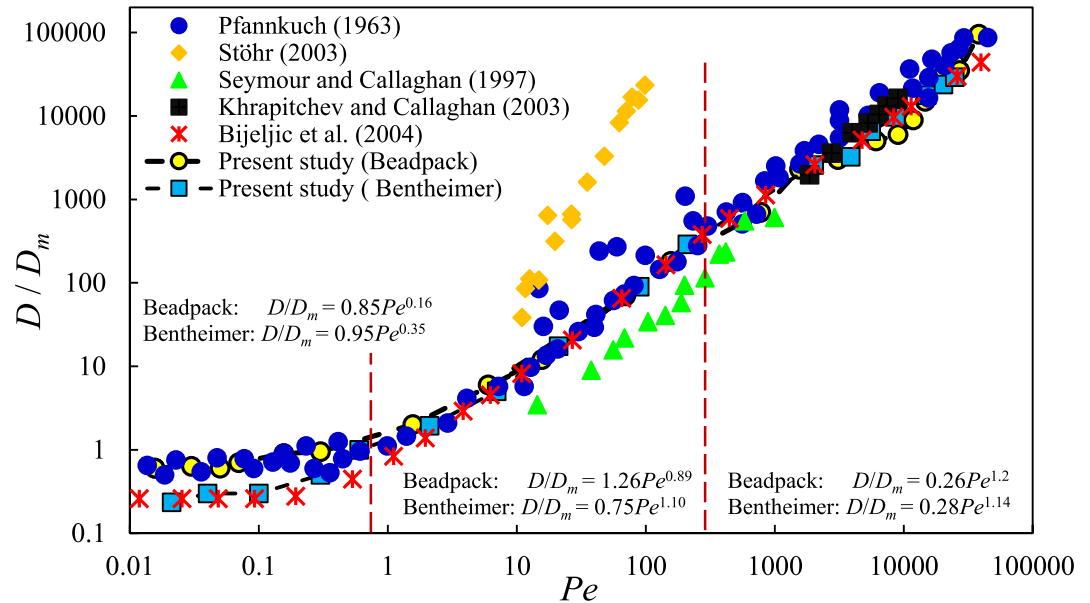
Figure 6. Normalized estimates of the (macro-scale) dispersion coefficient obtained through Maximum Likelihood at 25 values of the Péclet number spanning Darcy and Forchheimer regimes for the Beadpack and Bentheimer sandstone. As a term of comparison, results obtained through available (experimental and numerical) analyses for both samples are also depicted. Interpretation of the results through a power-law formulation of the kind $D/D_m = \alpha\,Pe^\delta$ are also included for both porous media samples.

$$D/D_m = \alpha\,\mathrm{Pe}^\delta \tag{10}$$

Beadpack: Pe < 1: $0.85\mathrm{Pe}^{0.16}$, 1 < Pe < 500: $1.26\mathrm{Pe}^{0.89}$, Pe > 500: $0.1\mathrm{Pe}^{1.32}$

Bentheimer: Pe < 1: $0.95\mathrm{Pe}^{0.35}$, 1 < Pe < 500: $0.75\mathrm{Pe}^{1.10}$, Pe > 500: $0.28\mathrm{Pe}^{1.14}$

These results (also depicted in Figure 6 for completeness) suggest that the power-law exponent (δ) is a function of the strength of the feedback between pore-scale diffusive and advective mechanisms. The value of δ increases dramatically in the presence of higher Péclect numbers, where advection effects become dominant. This supports the key relevance of the impact of advection on the dispersion of the scalar field across heterogeneous pore spaces. It is important to highlight that using separate models allows us to capture the dispersion variation in each flow regime. By estimating different values of α and δ for each regime, we can quantify the impact of flow nonlinearities on scalar dispersive transport. It is otherwise noted that the evolution of the system across different regimes might take place over a range of values of Péclet number rather than at a well-defined value. While the latter element would require additional investigations, it is otherwise clear that the dispersion behavior in the Darcy-, Transition-, and Forchheimer- regimes exhibits significant differences. This further underscores the critical role of pore-scale studies in analyzing these variations for each flow regime.

The influence of flow nonlinearity on dispersive transport is observed qualitatively in the scalar field distribution across two-dimensional cross-sections of the samples. Figures 7 and 8 depict exemplary pore velocities and scalar concentrations (normalized with respect to initial concentration and average velocity, respectively) at selected cross-sections along the average flow direction (i.e., $z = 0.3$ and $z = 0.75$ mm) for the Beadpack and Bentheimer samples, respectively, at the time the scalar first reaches the downstream boundary of the domain. These results enable one to visualize flow and scalar transport patterns, as influenced by the spatial heterogeneity of the system at various values of the Péclet number in the Darcy and Forchheimer regimes. A first appraisal of the effects of flow nonlinearity on scalar dispersion can be given upon comparison of the results depicted in Figures 7a and 7b for the Beadpack sample and Figures 8a and 8b for the Bentheimer sandstone system. The (normalized) pore-scale velocity fields display a structure which is more complex and characterized by higher local velocity gradients in the Forchheimer than in the Darcy regime for both samples. This behavior has a direct influence on scalar migration and, ultimately, on macro-scale dispersion. Visual comparison of Figures 7c–7f and Figures 8c–8f reveals the
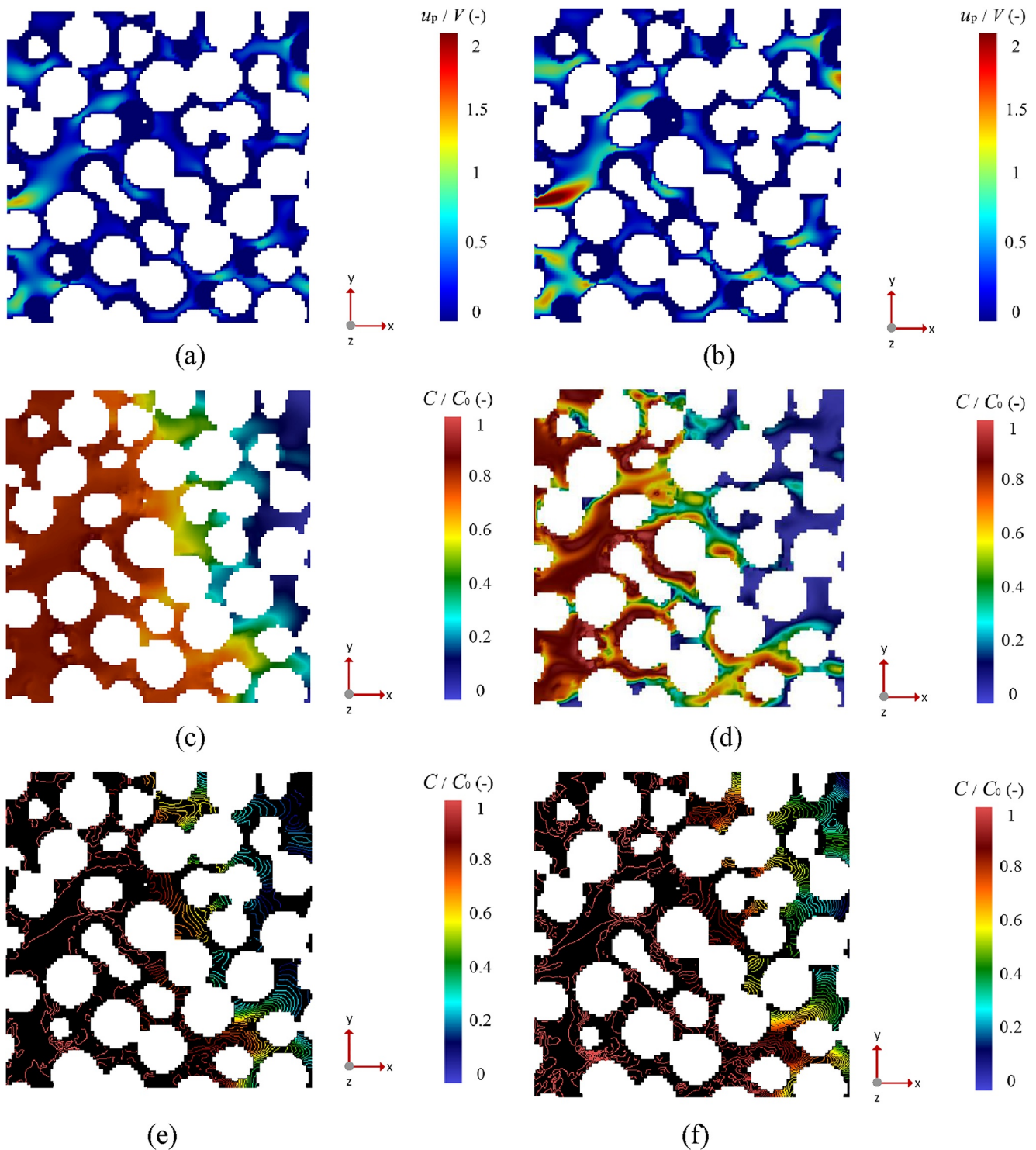
Figure 7. Color maps of pore-scale velocity and concentrations together with contour plots of concentrations for the Beadpack sample along the main flow direction at cross-sections identified by $z = 0.3$ mm: velocity field at Pe = (a) 0.015 and (b) 40,000; scalar field at Pe = (c) 0.015 and (d) 40,000; scalar field contour plots at Pe = (e) 0.015 and (f) 40,000.

influence of the complexity and degree of spatial heterogeneity of the pore space on scalar migration and dispersion. Consistent with the enhanced heterogeneity of the Bentheimer sandstone medium, scalar fields therein are associated with a more complex and irregular concentration gradient pattern (see Figures 8d and 8f). These observations are in line with previously documented results (see, e.g., Mousavi Nezhad et al., 2011; Yang et al., 2016),
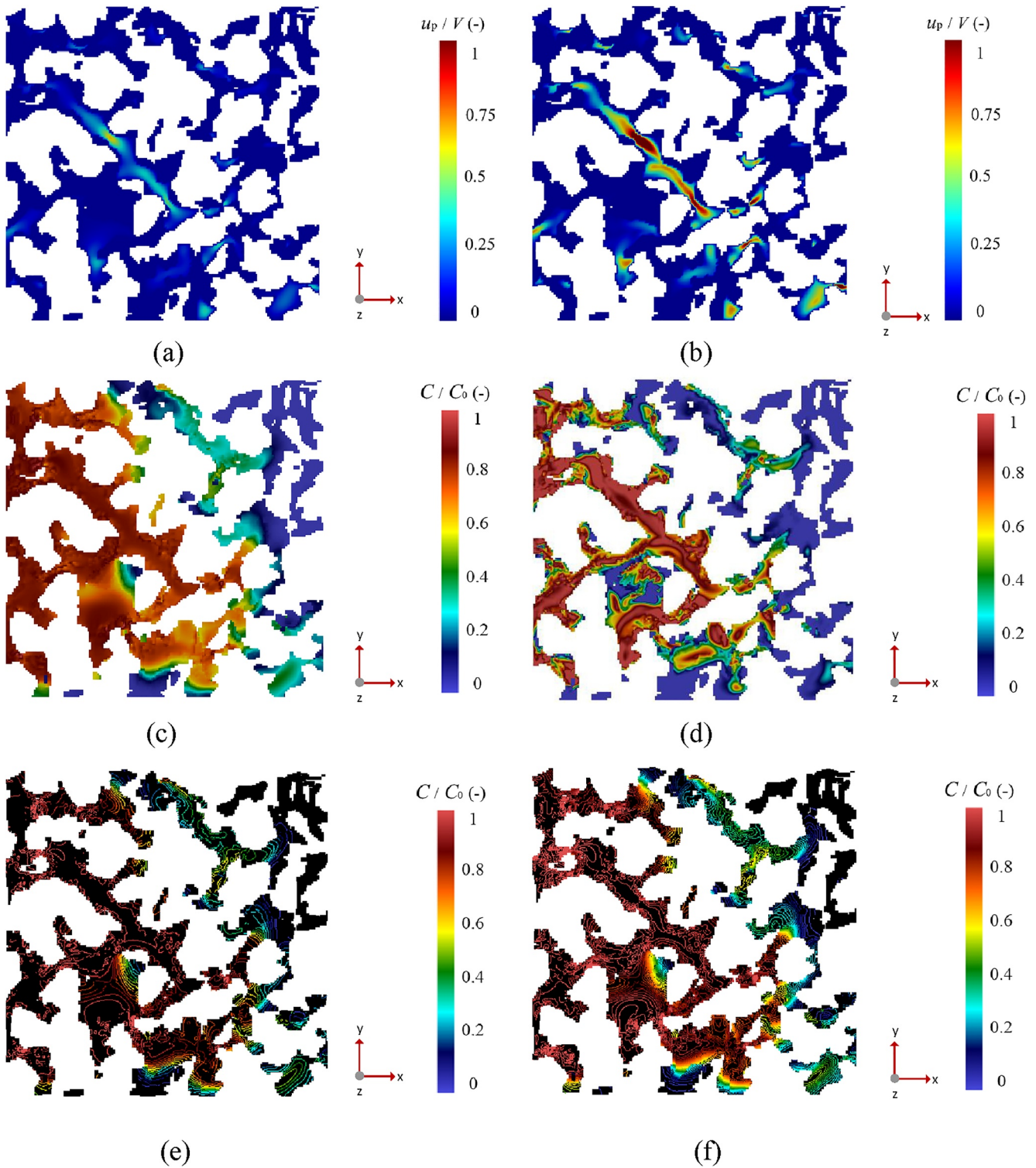
Figure 8. Color maps of pore-scale velocity and concentrations together with contour plots of concentrations for the Bentheimer sandstone sample along the main flow direction at cross-sections identified by $z = 0.75$ mm: velocity field at Pe = (a) 0.022 and (b) 24,825; scalar field at Pe = (c) 0.022 and (d) 24,825; scalar field contour plots at Pe = (e) 0.022 and (f) 24,825.
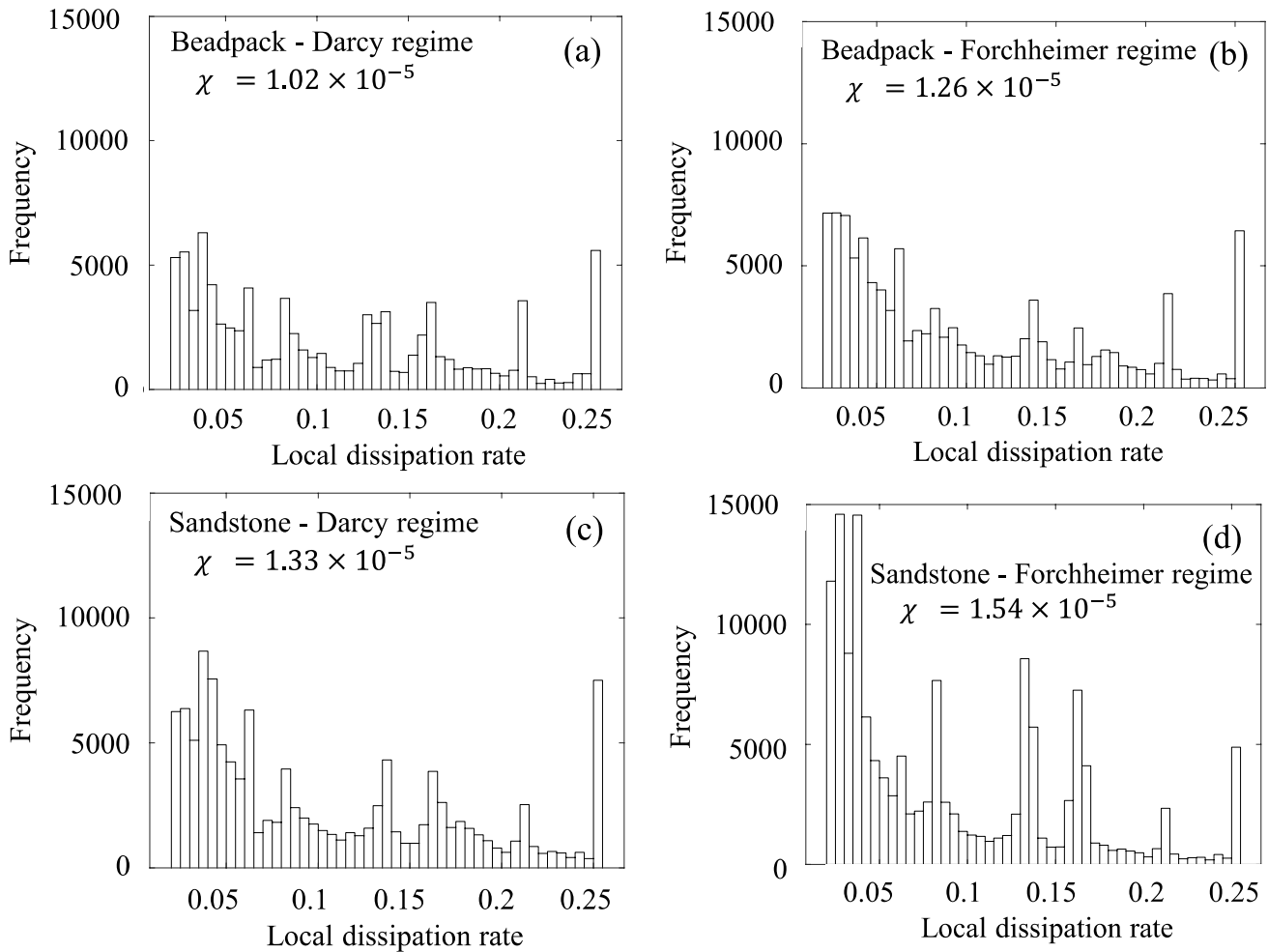
Figure 9. Histograms of local scalar dissipation rate evaluated across the Beadpack ((a) Darcy and (b) Forchheimer regime) and the Bentheimer sandstone ((c) Darcy and (d) Forchheimer regime) samples. Results correspond to the depictions offered in Figures 7 and 8. A threshold equal to 0.02 has been imposed to (normalized) concentrations to remove numerical results associated with zero or nearly zero concentration values.

where localized regions characterized by high concentration values are observed. These, in turn, correspond to an increase of the dispersion parameter and of the degree of complexity of the spatial distribution of concentration values. Visual inspection of Figures 7d and 7f and Figures 8d and 8f reveals the impact of pore structure heterogeneity on the scalar transport complexity and document that dispersion is significantly enhanced in the Forchheimer regime. When investigating scalar transport in heterogeneous porous media using pulse injection of solutes, some studies often rely on breakthrough curves (BTCs) to showcase the time-varying behavior of solute transport. By analyzing tailing behavior of the ensuing BTCs, these works reveal limitations of classical approaches in interpreting these types of section-averaged (upscaled) representations of transport processes across such media. While these studies have offered valuable insights, our work is mainly focused on analyzing the spatial complexity of the flow and scalar fields at the pore level in the presence of overall linear and nonlinear flow regimes. The snapshots associated with Figures 7 and 8 provide a clear appraisal of the complexity of the scalar field. The latter is tied to the degree of heterogeneity of the pore space as well as to the strength of flow nonlinearity. These elements emphasize the critical role of pore-scale analyses in enhancing our knowledge of the key traits of transport phenomena (see also, e.g., Batany et al., 2019; or de Winter et al., 2021; and references therein).

Figure 9 depicts the frequency distribution of the scalar dissipation rate described by $\mathfrak{x}(t) = 2D_m \nabla c(\mathbf{x}, t) . \nabla c(\mathbf{x}, t)$ (here, $\mathbf{x}$ corresponds to a two-dimensional position vector associated with coordinates x and y within a given cross-section), these results corresponding to those depicted in Figures 7 and 8 and being related to a measure of the mixing rate. The scalar dissipation rate is a measure of the rate at which a scalar quantity is mixed and dispersed
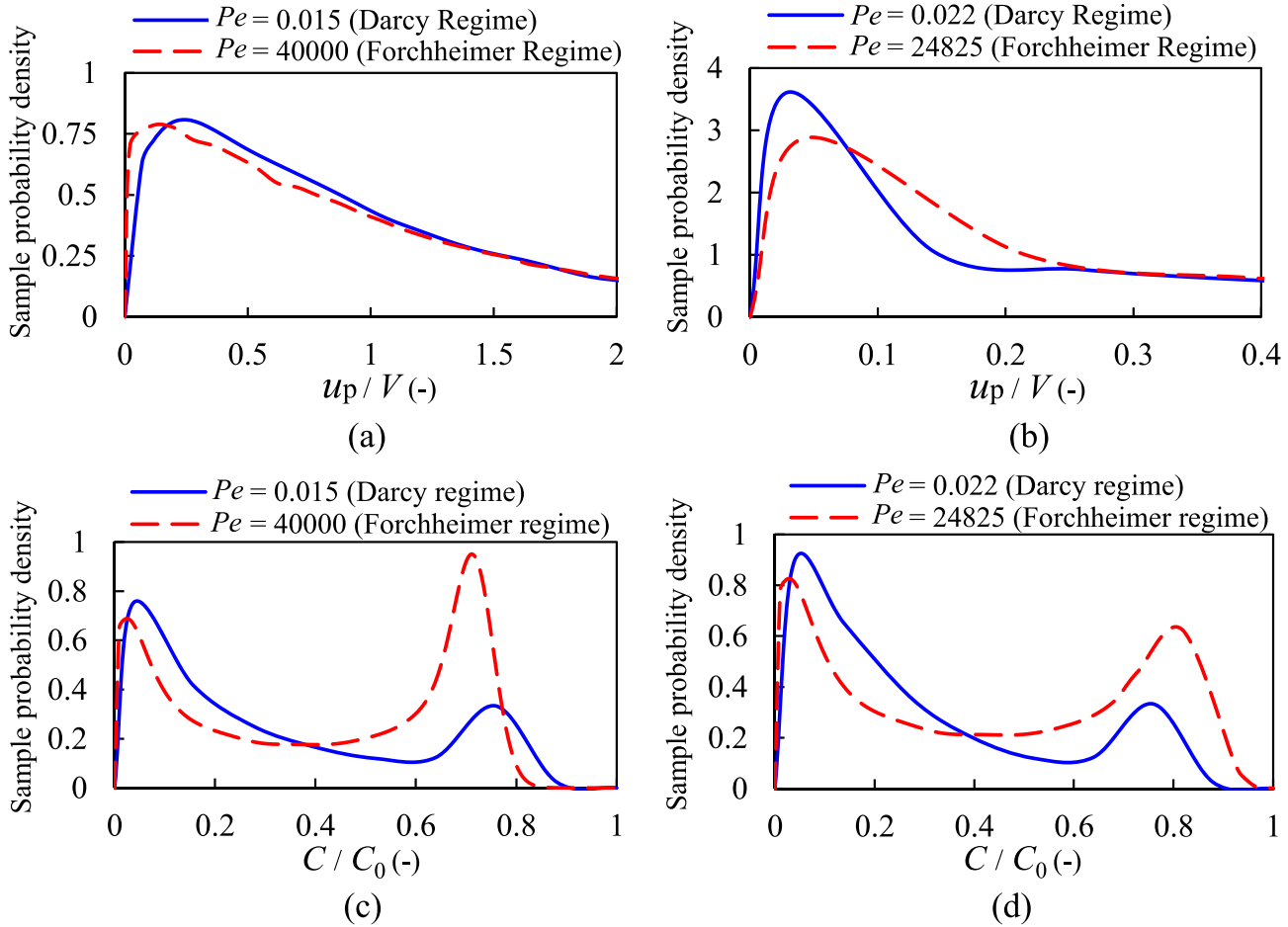
Figure 10. Sample probability density functions for pore-scale velocity norm ((a) Beadpack; (b) Bentheimer sandstone) and concentration ((c) Beadpack; (d) Bentheimer sandstone) fields for the Darcy and Forchheimer regimes associated with cross-sections depicted in Figures 7 and 8.

in a fluid flow. In other words, it represents the rate at which the scalar field is diffused and smoothed out by the turbulence in the flow (Bao et al., 2023; Wandel, 2023). These frequency distributions reveal that the Forchheimer regime is generally characterized by more locations where non-zero local concentration gradients can be found than the Darcy-flow regime, even as there is a considerable number of occurrences of very small gradient values (see, e.g., Figure 9d). Spatial heterogeneities of local gradients of concentrations are consistent with the significant increment of the dispersion coefficient observed in the Forchheimer flow regime. The increased values of the total dissipation rate, $\chi = \int 2D_m \nabla c(\boldsymbol{x},t).\nabla c(\boldsymbol{x},t)d\Omega$, at the cross-sections shown in Figures 7 and 8 support a conceptual picture according to which a Forchheimer regime is associated with enhanced scalar mixing.

To quantify the influence of velocity distributions on scalar transport, sample probability densities of the Eulerian (normalized) pore-scale velocity norm and concentration fields corresponding to Figures 7 and 8 are depicted in Figure 10. Pore-scale velocity fields across each sample are normalized through the corresponding average magnitude of the x component of the velocity. Results depicted in Figure 10 show that concentrations of the scalar field are characterized by a bimodal density function for both samples. Long decreasing limbs of the densities associated with intermediate times (i.e., in between the two peaks of the density) are consistent with the presence of several stagnant zones distributed across the domain. Values of Skewness and Kurtosis (see also Table 2) of sample densities of the scalar field indicate that tails tend to be heavier in the Forchheimer than in the Darcy regime. This is in

Table 2
Estimates of Skewness and Kurtosis Associated With the Sample Density Functions of the Velocity and Scalar Concentrations Corresponding to the Results Depicted in Figures 7 and 8 for the Darcy and Forchheimer Regimes Across the Two Porous Media Investigated

Heterogeneous sample	Beadpack sample		Bentheimer sandstone	
Statistical parameter	Skewness	Kurtosis	Skewness	Kurtosis
Darcy velocity field	1.548	6.53	1.822	8.019
Forchheimer velocity field	1.762	9.119	1.942	11.608
Darcy scalar field	−0.148	1.360	−0.213	1.934
Forchheimer scalar field	−0.293	2.945	−0.432	3.491

turn reflected onto the increased dispersion documented for the Forcheimer regime. The relative strengths of the peaks associated with high and low (normalized) concentrations suggest that effects of high velocity regions are dominant in the Forcheimer regime while the presence of regions associated with low velocities (i.e., virtually stagnant regions) are markedly important in driving scalar concentrations in the Darcy regime.
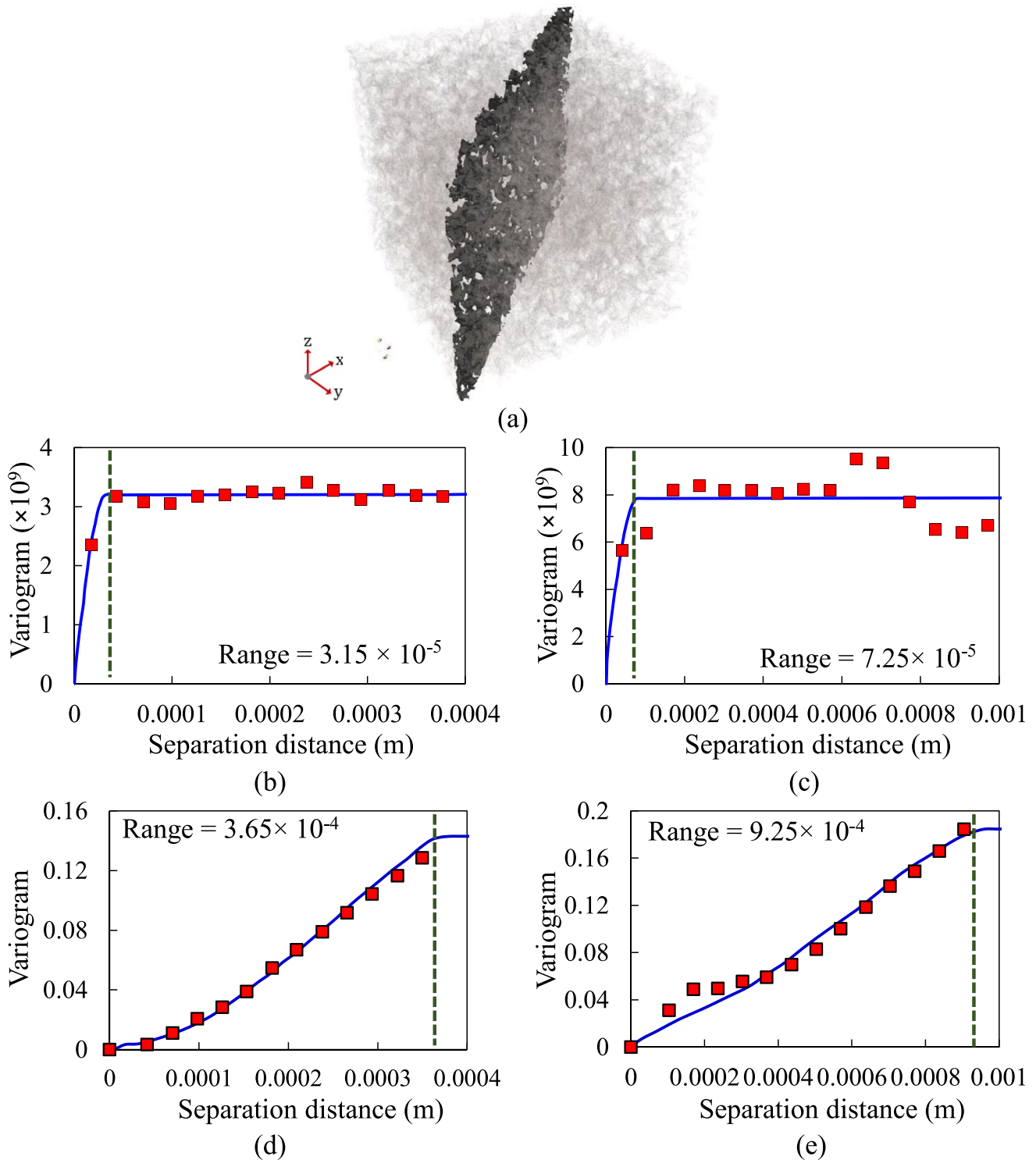
Figure 11 depicts sample variograms associated with pore-scale velocity and concentration fields (at time 0.01 and 0.006 s since the beginning of the simulation for Beadpack and Bentheimer, respectively) evaluated across a diagonal cross-section (see Figure 11e). The latter enables one to quantify the degree of spatial autocorrelation of velocity and scalar field data sets. This contributes to enrich our assessment of the influence of the heterogeneous pore space structure on the structure of velocity and scalar fields. For completeness, Figure 11 also includes corresponding theoretical interpretive variogram models. For completeness, Figure 11 also includes corresponding theoretical interpretive variogram models. These have been calibrated through Maximum Likelihood. In this particular case, we found that a spherical variogram model appears to best interpret the spatial structure of the velocity fields and the Gaussian model renders the best interpretation for the variogram of the scalar field. Estimates of variogram integral length scale for pore velocities are about 3.15×10^{-5} and 7.25×10^{-5} m (with associated velocity variances of 3.3×10^{-9} and 7.9×10^{-9}) for the Beadpack and Bentheimer sample, respectively. Otherwise, estimates of the corresponding integral scales for the scalar field are about 3.65×10^{-4} and 9.25×10^{-5} m (with associated scalar variances of 0.14 and 0.18) for the Beadpack and Bentheimer samples, respectively. Resting on the concept of scalar spreading proposed by Le Borgne et al. (2010), the variance of the scalar field is employed as an index to quantify the level of spreading. The results depicted in Figure 11 clearly illustrate that an increased heterogeneity of the pore space structure yields an overall enhancement of the variance of the pore velocity and of the scalar field (as expressed by the variogram sill). This also corresponds to an increased spreading of the scalar field across the more heterogeneous pore space. The strength of spatial correlation of the scalar concentration fields is observed to decrease in the nonlinear regime, consistent with the increased level of system heterogeneity.

3.3. Multi-Scale Analysis

We devote this Section to complement the results described in Section 3.1 upon analyzing and comparing main patterns of flow and scalar fields (and the associated relevant parameters) in various subregions across the systems, single pore volumes, and overall scales of observations.

We start by considering the three equally spaced sub-regions depicted in Figure 12 and analyze and compare degrees of flow nonlinearity and ensuing scalar dispersion as a function of the spatial heterogeneity therein (with the thickness of 60 and 150 μm for Beadpack and Bentheimer, respectively). Quantitative results for the variance of the norm of pore-scale velocities across each of these regions and estimated scalar dispersion parameters (using Maximum Likelihood and resting on the data on the sub-volumes) are listed in Table 3 for both porous domains. These results document considerable differences in these quantities across each of the selected sub-regions, as an effect of the spatial heterogeneity across each of the observation windows considered. The contribution of the dispersion mechanism to scalar transport (as quantified through the value of the estimated dispersion parameters) does not display a clear (increasing or decreasing) trend with the location of the sub-region in the system. It is generally higher in the Bentheimer sandstone sample, with the exception of Sub-region S2. These results suggest that flow and scalar transport behavior can markedly differ when considering different regions of a porous medium and various degrees of heterogeneity of the pore space. This further emphasizes the importance of fully embedding spatial fluctuations of flow at the smallest scales (i.e., scales smaller than those associated with the considered volumes) within large-scale models aiming at accurately capturing scalar transport phenomena across Darcy- and Forcheimer flow regimes.

Figure 13 depicts the sample density of the normalized norm of Eulerian pore velocities evaluated across regions whose extent is associated with various pore volumes across the system (also depicted in Figure 13). These analyses enable us to assess the way statistical features of the pore-scale velocities vary across the heterogeneous system, thus giving rise to a spatially varying strength of the scalar spreading. Sample PDFs of the velocity fields of the selected exemplary pore volumes vary spatially due to the heterogeneity of the system and differ from their counterpart evaluated across the whole sample (see Figure 10). One can observe that differences amongst the sample densities associated with the selected pore volumes is higher in the Forchheimer regime. This result is consistent with a conceptual picture according to which changes in the local behavior of the flow field tend to become more markedly visible as Re_l increases and the macro-scale system behavior becomes nonlinear. It is

Figure 11. Sample variograms (and corresponding interpretive models) associated with (b) and (c) pore-scale velocity and (d) and (e) concentration fields evaluated across the diagonal cross-section depicted at time 0.01 and 0.006 s since the beginning of the simulation for Beadpack and Bentheimer, respectively. Results correspond to the same pressure gradient of 1 Mpa/m and are associated with Pe = 1,500 and 200 for the Beadpack and Bentheimer sandstone systems, respectively.

clear that pore velocity has a local behavior that varies significantly, in terms of its sample probability density, when considering different sampling regions of the porous system. One can note that values of the velocity at which the peak is attained in the sample PDFs differ across the volumes considered and that velocity values are
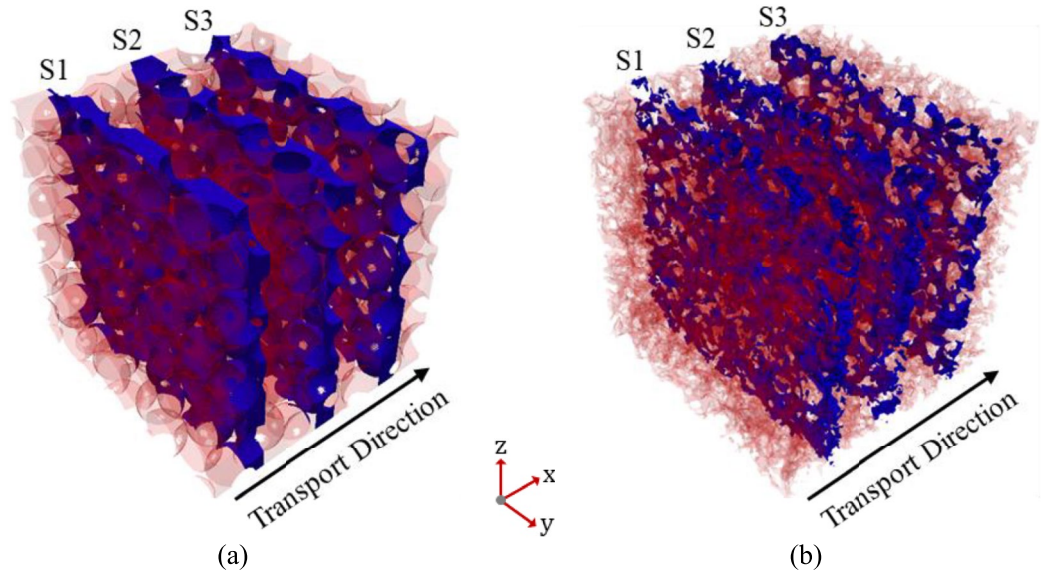
Figure 12. Sub-regions selected along the main flow direction within which local flow non-linearity and ensuing scalar dispersion are assessed and compared for (a) the Beadpack and (b) the Bentheimer sandstone sample. Pore spaces are highlighted in blue with the thickness of 60 and 150 μm for Beadpack and Bentheimer, respectively.

distributed across a broad range, especially for the more heterogeneous Bentheimer sandstone medium. In agreement with the results listed in Table 3, heavier tailing (as quantified through sample Skewness and Kurtosis) can be observed for the specified volumes under Forchheimer regimes.

Figures 14 and 15 complement the analysis upon providing an additional perspective based on the analysis of sample PDFs of the magnitude of pore velocities for different scales (denoted as ξ, representing the side of the cubic volumes depicted in the figure) within the Beadpack and Bentheimer sandstone samples, respectively. Sample PDFs of local velocity fields in the Forchheimer regime (see Figures 14g and 15g) further strengthens the importance of the scale of analysis in capturing the heterogeneous flow features that affect scalar transport mechanisms. Sample PDFs tend to become more right skewed as the size of sampling volume increases. This is in line with the increased importance of low (normalized) velocity values associated with virtually stagnant regions and an increase of the surface of the solid grains (at which velocity vanishes) encompassed in the sampling volume. Moreover, differences in the shapes of the sample PDFs evaluated at various scales are more significant for the Bentheimer sandstone, consistent with its enhanced pore space heterogeneity. Quantitative results of multi-scale velocity field analyses are listed in Table 4, including their mean and variance for each of the characteristic scales (ξ) assessed. Our results show lower variance and mean values for velocity fields of the larger simulation domain for the cases analyzed in this work. As stated above, this behavior is supported by the observation that for larger simulation domains the increased amount of small velocity values close to solid boundaries or within low velocity (or virtually stagnant) regions yield a reduction of the average velocity and of the population variance in our simulated cases.

Hydraulic tortuosity is also considered as a critical quantity for the characterization of the complexity of flow fields. Here, we determine hydraulic tortuosity for the Darcy and Forchheimer regimes upon relying on the fluid velocity field (see also Duda et al., 2011). The hydraulic tortuosity is evaluated as the ratio between the spatial average of the pore flow speed and the spatial average of the magnitude of the velocity component parallel to the Darcy-scale flow direction.

Hydraulic tortuosity is also considered as a critical quantity for the characterization of the complexity of flow fields. Figure 16 depicts the evaluated hydraulic tortuosity and permeability of the Beadpack and Bentheimer

Table 3
Standard Deviation of the Norm of the Pore-Velocity Associated With the Three Sub-Regions Depicted in Figure 12 and Maximum Likelihood Estimates (and Estimation Variance) of the Corresponding Dispersion Parameter

Subregions	Standard deviation of pore-scale velocities (m/s)	Estimated D (m²/s)	Estimation variance for D (m²/s)²
Beadpack sample			
Subregion S1	0.175	1.5E−05	4.8E−07
Subregion S2	0.324	3.5E−05	1.12E−06
Subregion S3	0.147	0.5E−05	1.6E−07
Bentheimer sandstone sample			
Subregion S1	0.254	2.0E−05	6.56E−05
Subregion S2	0.176	1.0E−05	3.28E−05
Subregion S3	0.425	4.5E−05	1.48E−04

Note. Results correspond to the same pressure gradient of 10 MPa and Pe = 14,000 or 15,000 for the Beadpack and Bentheimer sandstone samples.
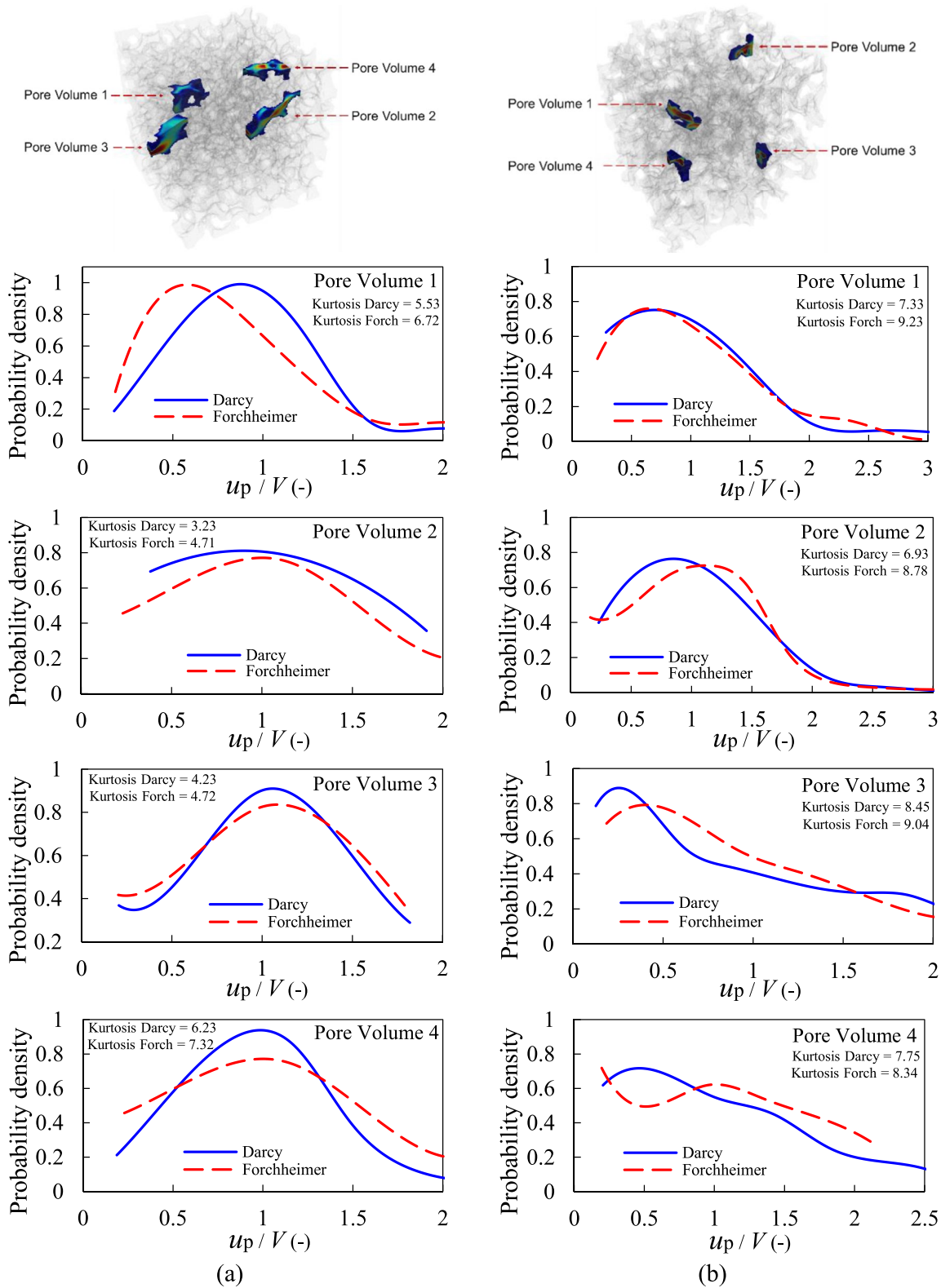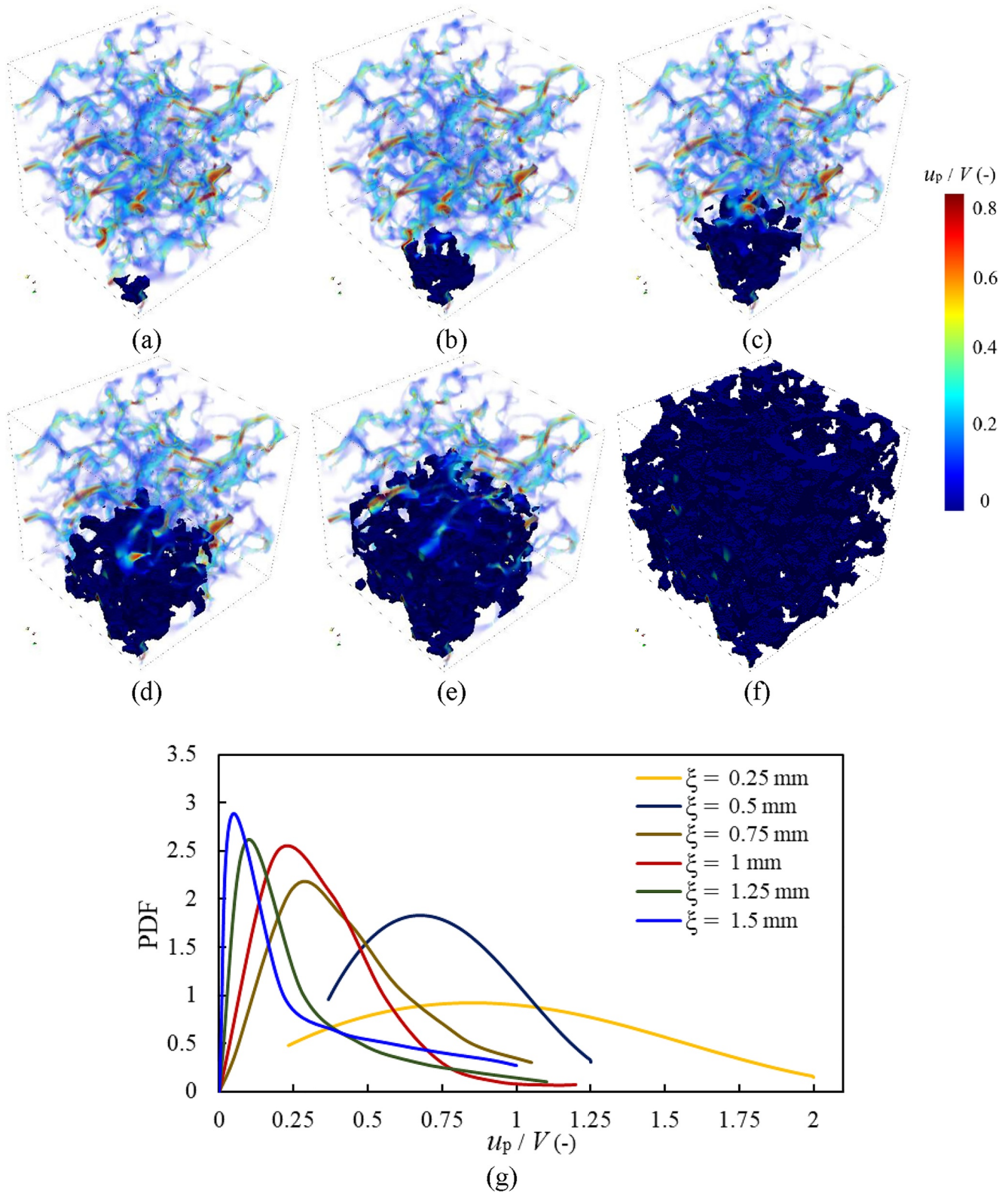
Figure 13. Sample probability density functions of the normalized norm of pore velocity in the Darcy and Forchheimer regimes for (a) the Beadpack (Pe = 0.015, Pe = 40,000) and (b) the Bentheimer sandstone (Pe = 0.022, Pe = 24,825) samples. Results are associated with the four volumes depicted, that are randomly selected across the systems. The size of selected pore volumes equals one percent of sample sizes (volume).
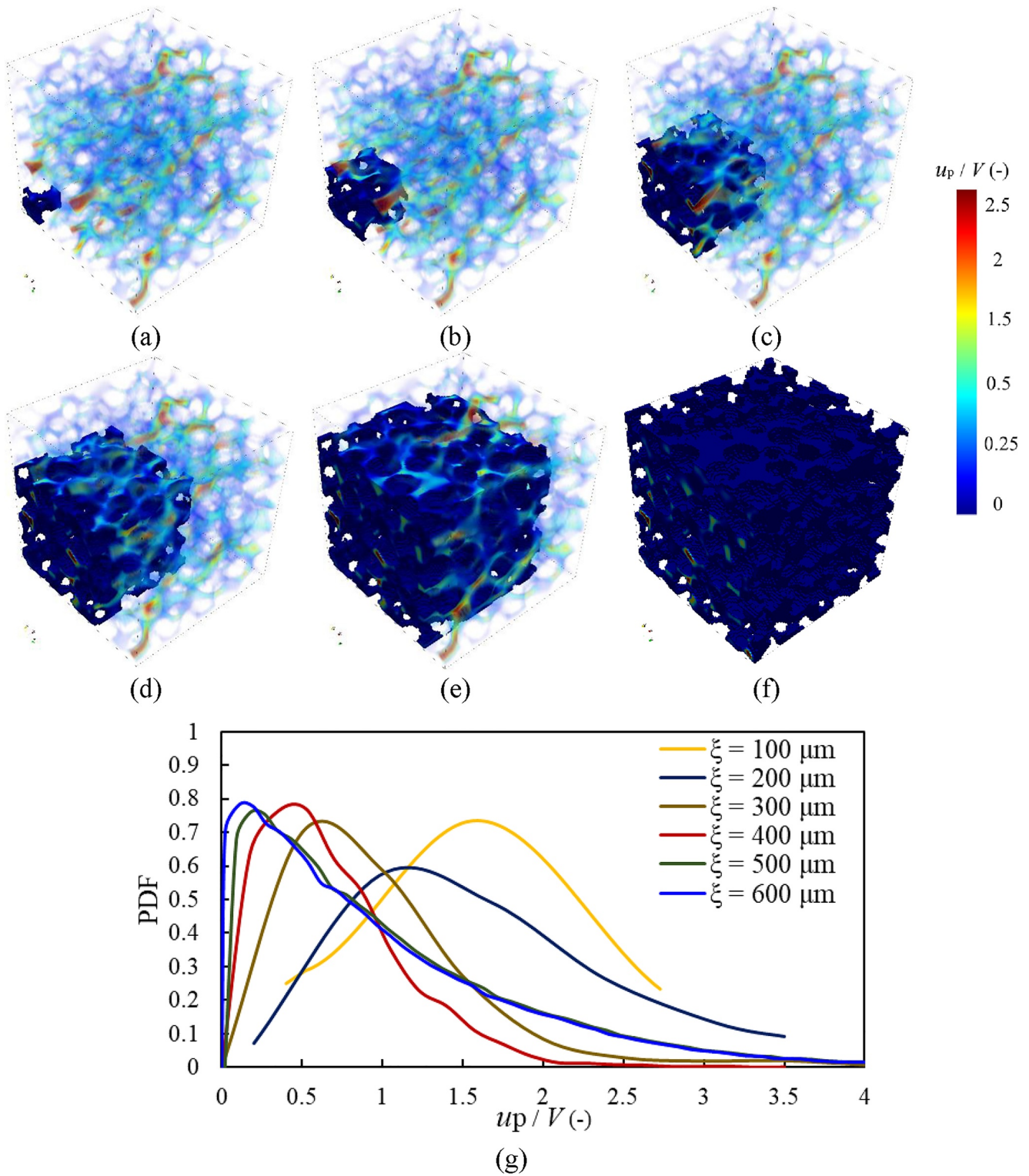
Figure 14. (g) Sample probability densities (PDFs) of normalized magnitude of velocities associated with the investigation volumes depicted and characterized by lengths ξ = (a) 100 μm, (b) 200 μm, (c) 300 μm, (d) 400 μm, (e) 500 μm, and (f) 600 μm. Results correspond to the Beadpack sample and Pe = 40,000 (Forchheimer regime).

Figure 15. (g) Sample probability densities (PDFs) of normalized magnitude of velocities associated with the investigation volumes depicted and characterized by lengths ξ = (a) 0.25 mm, (b) 0.50 mm, (c) 0.75 mm, (d) 1 mm, (e) 1.25 mm, and (f) 1.5 mm. Results correspond to the Bentheimer sandstone and Pe = 24,825 (Forchheimer regime).

Table 4
Mean and Standard Deviation of Pore-Scale Velocities as a Function of Cube Size Effect in the Forchheimer Regime (a) Beadpack at Pe = 40,000, (b) Bentheimer Sandstone at Pe = 24,825

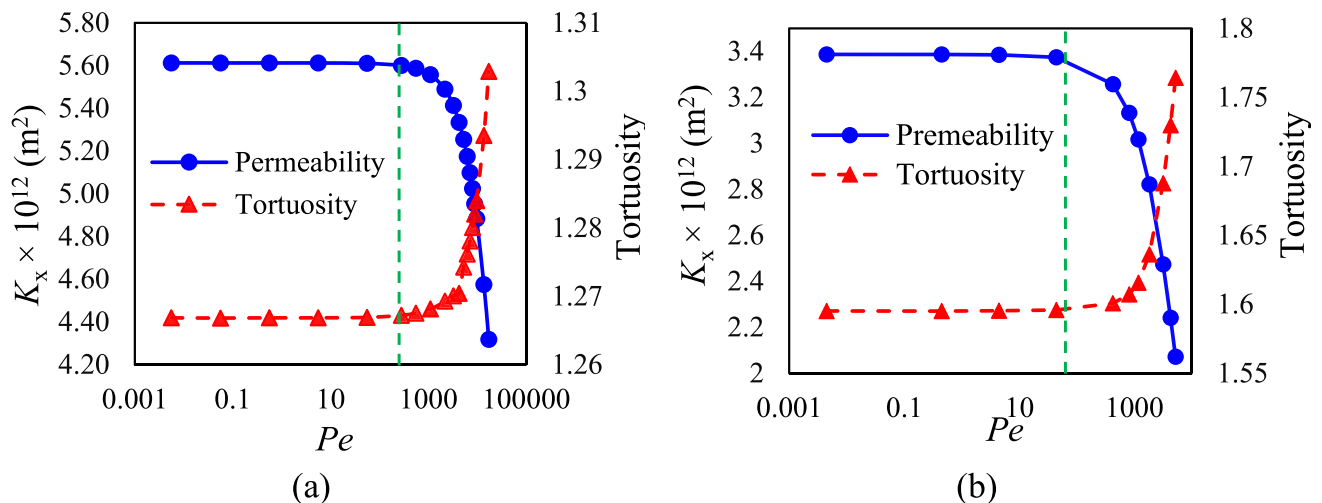| Beadpack sample			Bentheimer sandstone		
Scale ξ (μm)	Mean velocity (m/s)	Flow standard deviation (m/s)	Scale ξ (mm)	Flow mean (m/s)	Flow standard deviation (m/s)
100	0.2535	0.1969	0.25	0.3521	0.3542
200	0.2297	0.1621	0.5	0.2710	0.2882
300	0.2182	0.1550	0.75	0.2202	0.2596
400	0.2093	0.1391	1	0.1758	0.1628
500	0.2034	0.1343	1.25	0.1692	0.1599
600	0.1973	0.1060	1.5	0.1517	0.1568

sandstone samples versus a wide range of values of Péclet number, Pe. One can note that hydraulic tortuosity displays a sharp increase when transitioning from a Darcy- to a Forchheimer- regime. This is consistent with the observation that nonlinearities of flow favor increased complexity. These results complement their counterparts depicted in Figure 6, where one can notice that flow complexity and higher hydraulic tortuosity promote increased dispersion of the scalar field for higher Péclet numbers. It can also be observed that the Bentheimer sandstone sample is characterized by a higher hydraulic tortuosity and level of transport complexity as a result of the higher complexity of the pore space as compared against the Beadpack sample.

4. Conclusions

We present a multi-scale analysis of the main features of dispersive scalar transport taking place across pore spaces associated with differing degrees of heterogeneity. We consider two frequently studied micro-scale porous media (i.e., a Beadpack and a Bentheimer sandstone) imaged through a close packing approach and X-ray CT and rest on detailed numerical simulations of pore-scale flow and transport therein. Our simulations encompass both linear (Darcy-) and nonlinear (Forchheimer) flow regimes and span across a wide range of values of Péclet number. Our work leads to the following major conclusions.

1. The pore-scale velocity fields are characterized by a spatial structure that is more complex and associated with enhanced local gradients in the Forchheimer than in the Darcy regime for both samples. In turn, flow taking place across the Bentheimer sandstone domain enters the (nonlinear) Forchheimer regime at a value of the Reynolds number which is lower than the corresponding one observed for the less heterogeneous Beadpack sample. This result is related to the different degrees of pore space heterogeneity of the two pore spaces.
2. Spatial distribution of the concentration of the migrating scalar are associated with a more complex and irregular concentration gradient pattern in the Bentheimer sandstone than in the Beadpack sample. The Forchheimer flow regime is characterized by enhanced mixing of the scalar field which, in turn, leads to larger dispersion than in the Darcy regime.
3. Concentration densities are characterized by a bimodal behavior for both samples. This is consistent with the presence of stagnant zones distributed across the domain as well as dominant preferential flow conduits. The relative strengths of the peaks associated with high and low (normalized) concentrations suggest that the effects of high velocity regions are dominant in the Forcheimer regime. Otherwise, the Darcy regime is characterized by a high relative importance of low velocity regions in governing concentration distributions.


Figure 16. Hydraulic tortuosity and permeability versus the Péclet number for the (a) Beadpack and (b) Bentheimer sandstone samples. The vertical green line shows the onset of the Forchheimer regime for both porous domains.

4. Estimated values of dispersion associated with section-averaged breakthrough curves display a power-law scaling on the Péclet number. The strength of the scaling exponent depends on the relative importance of pore-scale diffusive and advective mechanisms. Advection mechanisms dominate when flow is associated with an (overall nonlinear) Forchheimer regime (i.e., $Pe > 500$).
5. Sample PDFs of velocity and concentrations evaluated at various scales display differences that are more significant for the most heterogeneous porous domain.

Thus, our results suggests that it is critical to incorporate the pore-scale and local features of the flow field in the dispersive transport and mixing models when considering non-Darcy flow regimes.

Appendix A: Mesh Generation

As presented in Figure A1, the three-dimensional mesh domains with high accuracy are generated for the Bead-pack sample and Bentheimer sandstone. Generated mesh domains capture all pores, void spaces, and solid-void

Three-Dimensional mesh domain   Two-Dimensional mesh domain   Two-Dimensional zoom-in mesh

(a)

Three-Dimensional mesh domain   Two-Dimensional mesh domain   Two-Dimensional zoom-in mesh

(b)
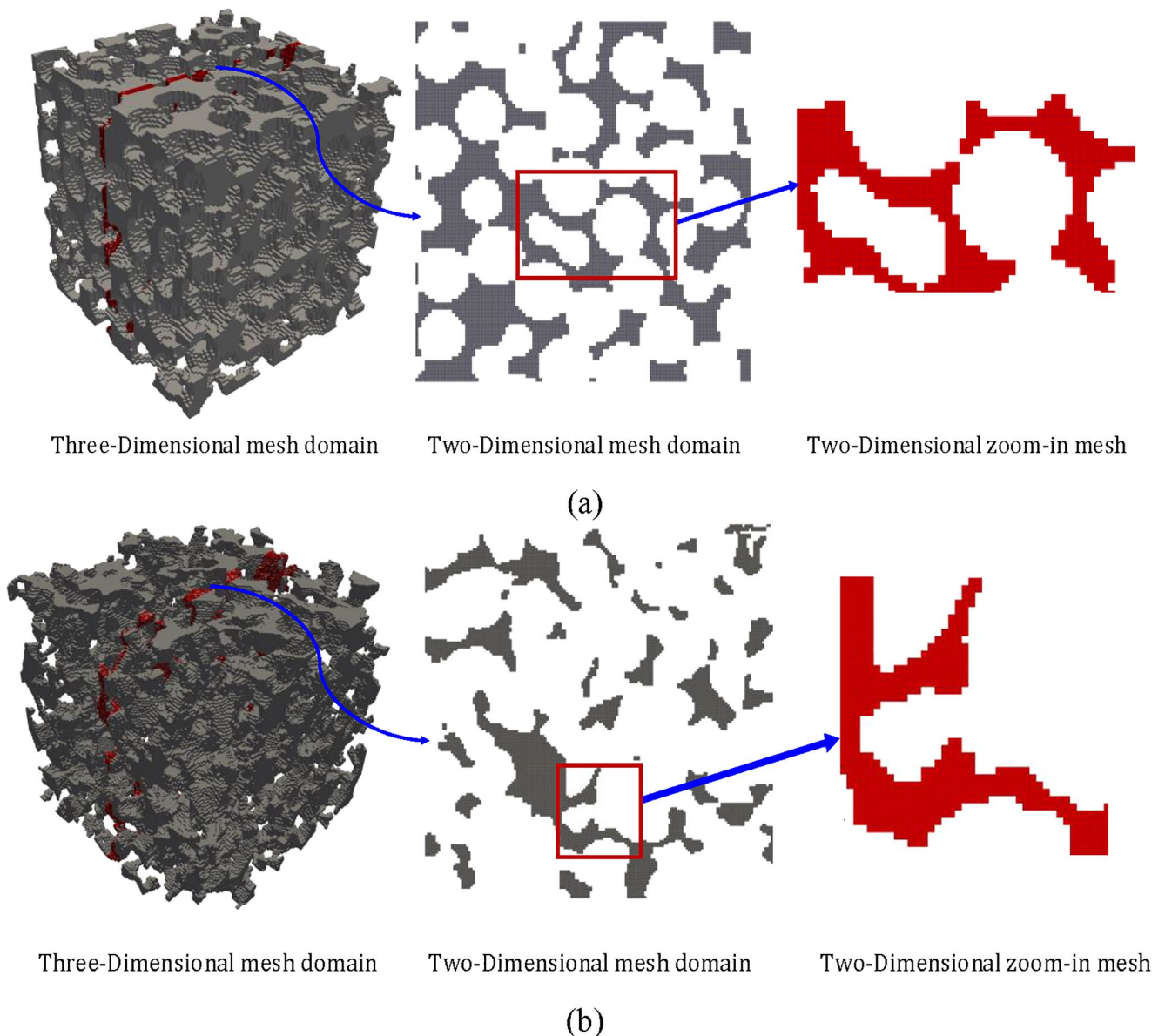
Figure A1. Computational domain generated by using SnappyHexMesh tool in the OpenFOAM platform for (a) Beadpack sample, (b) Bentheimer sandstone presenting 3D mesh domains.
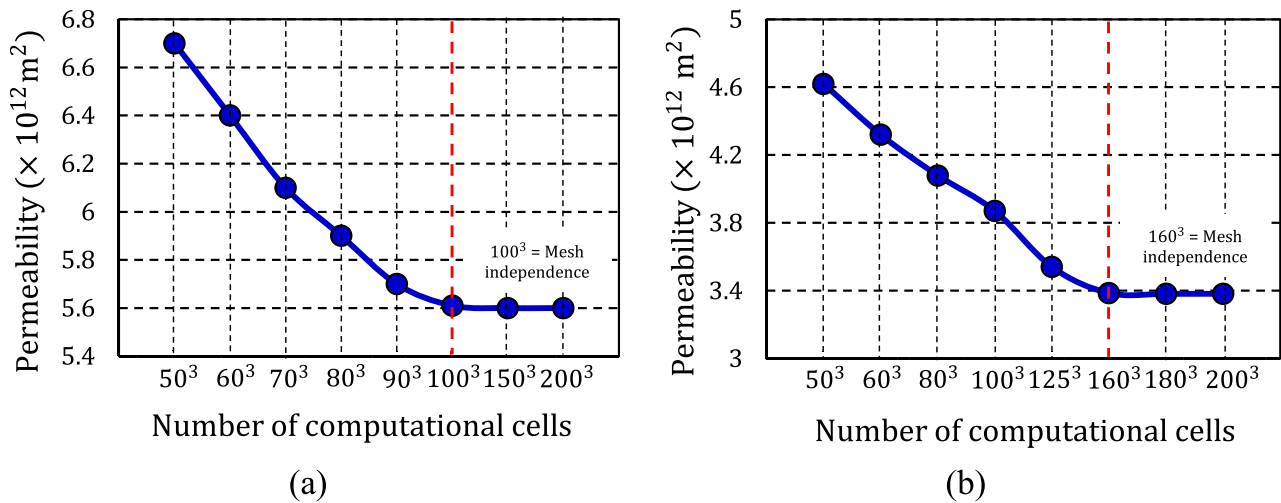
Figure A2. Plots representing independency of numerical simulation from computational domain cell numbers. (a) Beadpack sample, optimum mesh number = 100^3, (b) Bentheimer sandstone, optimum mesh number = 160^3.

interfaces in the porous domain quite clearly, which is essential for the accurate simulation of the heterogeneous porous samples.

Moreover, As presented in Figure A2, a detailed grid convergence study is performed to identify the optimal computational grids for both samples. The optimum computational grids for the Beadpack sample and Bentheimer sandstone are 100^3 and 160^3, respectively. Due to the higher heterogeneity and complexity of Bentheimer, this sample needs more computational cells to capture all intricacies and micro-structures in the porous media. All simulations rely on a workstation with 2 Intel® Xeon® CPUs (each including 16 threads @ 3.3 GHz) and 64 GB computational memory.

Data Availability Statement

SimpleFoam solver of the open-source CFD platform OpenFOAM (Jasak et al., 2007) used for the pore-scale flow and solute transport simulations is available via (https://openfoamwiki.net/index.php/SimpleFoam) and ScalarTransportFoam solver used for solute transport simulations is available via (https://openfoamwiki.net/index.php/ScalarTransportFoam).

References

Aramideh, S., Vlachos, P. P., & Ardekani, A. M. (2018). Pore-scale statistics of flow and transport through porous media. *Physical Review E*, *98*(1), 013104. https://doi.org/10.1103/PhysRevE.98.013104

Aziz, R., Joekar-Niasar, V., & Martinez-Ferrer, P. (2018). Pore-scale insights into transport and mixing in steady-state two-phase flow in porous media. *International Journal of Multiphase Flow*, *109*, 51–62. https://doi.org/10.1016/j.ijmultiphaseflow.2018.07.006

Bao, H., Akargun, H. Y., Roekaerts, D., & Somers, B. (2023). The inclusion of scalar dissipation rate in modeling of an n-dodecane spray flame using flamelet generated manifold. *Combustion and Flame*, *249*, 112610. https://doi.org/10.1016/j.combustflame.2022.112610

Batany, S., Peyneau, P.-E., Lassabatère, L., Béchet, B., Faure, P., & Dangla, P. (2019). Interplay between molecular diffusion and advection during solute transport in macroporous media. *Vadose Zone Journal*, *18*(1), 1–15. https://doi.org/10.2136/vzj2018.07.0140

Bijeljic, B., Muggeridge, A. H., & Blunt, M. J. (2004). Pore-scale modeling of longitudinal dispersion. *Water Resources Research*, *40*(11), W11501. https://doi.org/10.1029/2004wr003567

Blunt, M. J., Bijeljic, B., Dong, H., Gharbi, O., Iglauer, S., Mostaghimi, P., et al. (2013). Pore-scale imaging and modelling. *Advances in Water Resources*, *51*, 197–216. https://doi.org/10.1016/j.advwatres.2012.03.003

Delgado, J. (2007). Longitudinal and transverse dispersion in porous media. *Chemical Engineering Research and Design*, *85*(9), 1245–1252. https://doi.org/10.1205/cherd07017

de Winter, D. A. M., Weishaupt, K., Scheller, S., Frey, S., Raoof, A., Hassanizadeh, S. M., & Helmig, R. (2021). The complexity of porous media flow characterized in a microfluidic model based on confocal laser scanning microscopy and micro-PIV. *Transport in Porous Media*, *136*(1), 343–367. https://doi.org/10.1007/s11242-020-01515-9

Dong, S., Zhou, M., Su, X., Xia, J., Wang, L., Wu, H., et al. (2022). Transport and retention patterns of fragmental microplastics in saturated and unsaturated porous media: A real-time pore-scale visualization. *Water Research*, *214*, 118195. https://doi.org/10.1016/j.watres.2022.118195

Duda, A., Koza, Z., & Matyka, M. (2011). Hydraulic tortuosity in arbitrary porous media flow. *Physical Review E*, *84*(3), 036319. https://doi.org/10.1103/physreve.84.036319

El-Zehairy, A. A., Nezhad, M. M., Joekar-Niasar, V., Guymer, I., Kourra, N., & Williams, M. A. (2019). Pore-network modelling of non-Darcy flow through heterogeneous porous media. *Advances in Water Resources*, *131*, 103378. https://doi.org/10.1016/j.advwatres.2019.103378

Gaiselmann, G., Neumann, M., Schmidt, V., Pecho, O., Hocker, T., & Holzer, L. (2014). Quantitative relationships between microstructure and effective transport properties based on virtual materials testing. *AIChE Journal*, *60*(6), 1983–1999. https://doi.org/10.1002/aic.14416

Guadagnini, A., & Neuman, S. P. (2001). Recursive conditional moment equations for advective transport in randomly heterogeneous velocity fields. *Transport in Porous Media*, *42*(1/2), 37–67. https://doi.org/10.1023/a:1006791809883

Huang, J., Xiao, F., Dong, H., & Yin, X. (2019). Diffusion tortuosity in complex porous media from pore-scale numerical simulations. *Computers & Fluids*, *183*, 66–74. https://doi.org/10.1016/j.compfluid.2019.03.018

Icardi, M., Boccardo, G., Marchisio, D. L., Tosco, T., & Sethi, R. (2014). Pore-scale simulation of fluid flow and solute dispersion in three-dimensional porous media. *Physical Review E*, *90*(1), 013032. https://doi.org/10.1103/physreve.90.013032

Jasak, H., Jemcov, A., & Tukovic, Z. (2007). OpenFOAM: A C++ library for complex physics simulations. *International workshop on coupled methods in numerical dynamics* (Vol. 1000, pp. 1–20). IUC Dubrovnik Croatia.

Khrapitchev, A. A., & Callaghan, P. T. (2003). Reversible and irreversible dispersion in a porous medium. *Physics of Fluids*, *15*(9), 2649–2660. https://doi.org/10.1063/1.1596914

Le Borgne, T., Dentz, M., Bolster, D., Carrera, J., de Dreuzy, J. R., & Davy, P. (2010). Non-Fickian mixing: Temporal evolution of the scalar dissipation rate in heterogeneous porous media. *Advances in Water Resources*, *33*(12), 1468–1475. https://doi.org/10.1016/j.advwatres.2010.08.006

Metcalfe, G., Lester, D., & Trefry, M. (2022). A primer on the Lagrangian picture of transport in porous media. *ArXiv:2202.13053 [Nlin, Physics:Physics]*. http://arxiv.org/abs/2202.13053

Moghimi, H., Siavashi, M., Mousavi Nezhad, M., & Guadagnini, A. (2022). Pore-scale computational analyses of non-Darcy flow through highly porous structures with various degrees of geometrical complexity. *Sustainable Energy Technologies and Assessments*, *52*, 102048. https://doi.org/10.1016/j.seta.2022.102048

Mostaghimi, P., Blunt, M. J., & Bijeljic, B. (2013). Computations of absolute permeability on micro-CT images. *Mathematical Geosciences*, *45*(1), 103–125. https://doi.org/10.1007/s11004-012-9431-4

Mousavi Nezhad, M., & Javadi, A. A. (2011). Stochastic finite-element approach to quantify and reduce uncertainty in pollutant transport modeling. *Journal of Hazardous, Toxic, and Radioactive Waste*, *15*(3), 208–215. https://doi.org/10.1061/(ASCE)HZ.1944-8376.0000055

Mousavi Nezhad, M., Javadi, A. A., & Rezania, M. (2011). Modeling of contaminant transport in soils considering the effects of micro- and macro-heterogeneity. *Journal of Hydrology*, *404*(3), 332–338. https://doi.org/10.1016/j.jhydrol.2011.05.004

Muljadi, B. P., Blunt, M. J., Raeini, A. Q., & Bijeljic, B. (2016). The impact of porous media heterogeneity on non-Darcy flow behavior from pore-scale simulation. *Advances in Water Resources*, *95*, 329–340. https://doi.org/10.1016/j.advwatres.2015.05.019

Müller, S., Schüler, L., Zech, A., & Heße, F. (2021). GSTools v1. 3: A toolbox for geostatistical modelling in Python. *Geoscientific Model Development Discussions*, *2021*, 1–33.

Mousavi Nezhad, M., Rezania, M., Rezania, M., & Baioni, E. (2019). Transport in porous media with nonlinear flow condition. *Transport in Porous Media*, *126*(1), 5–22. https://doi.org/10.1007/s11242-018-1173-4

Pfannkuch, H.-O. (1962). Contribution a Ietude des deplacement de fluids miscible dans un milieu poreux. *Revue de l'Institut Français du Petrole*, *18*(2), 215–270.

Poureslami, P., Siavashi, M., Moghimi, H., & Hosseini, M. (2021). Pore-scale convection-conduction heat transfer and fluid flow in open-cell metal foams: A three-dimensional multiple-relaxation time lattice Boltzmann (MRT-LBM) solution. *International Communications in Heat and Mass Transfer*, *126*, 105465. https://doi.org/10.1016/j.icheatmasstransfer.2021.105465

Prodanović, M., & Bryant, S. L. (2006). A level set method for determining critical curvatures for drainage and imbibition. *Journal of Colloid and Interface Science*, *304*(2), 442–458. https://doi.org/10.1016/j.jcis.2006.08.048

Sadeghi, M. A., Agnaou, M., Barralet, J., & Gostick, J. T. (2020). Dispersion modeling in pore networks: A comparison of common pore-scale models and alternative approaches. *Journal of Contaminant Hydrology*, *228*, 103578. https://doi.org/10.1016/j.jconhyd.2019.103578

Seymour, J. D., & Callaghan, P. T. (1997). Generalized approach to NMR analysis of flow and dispersion in porous media. *AIChE Journal*, *43*(8), 2096–2111. https://doi.org/10.1002/aic.690430817

Stöhr, M. (2003). Analysis of flow and transport in refractive index matched porous media (PhD Thesis).

Talon, L., Ollivier-Triquet, E., Dentz, M., & Bauer, D. (2023). Transient dispersion regimes in heterogeneous porous media: On the impact of spatial heterogeneity in permeability and exchange kinetics in mobile–immobile transport. *Advances in Water Resources*, *174*, 104425. https://doi.org/10.1016/j.advwatres.2023.104425

Thakur, C., Swami, D., & Joshi, N. (2022). Experimental and numerical investigation of evaluation of grain size–based porosity models for solute transport through porous medium. *Journal of Hazardous, Toxic, and Radioactive Waste*, *26*(2), 04021059. https://doi.org/10.1061/(ASCE)HZ.2153-5515.0000660

Van Offenwert, S., Cnudde, V., Boone, M., & Bultreys, T. (2021). Fast micro-computed tomography data of solute transport in porous media with different heterogeneity levels. *Scientific Data*, *8*(1), 1–8. https://doi.org/10.1038/s41597-021-00803-3

Van Offenwert, S., Cnudde, V., & Bultreys, T. (2019). Pore-scale visualization and quantification of transient solute transport using fast micro-computed tomography. *Water Resources Research*, *55*(11), 9279–9291. https://doi.org/10.1029/2019wr025880

Vasheghani Farahani, M., Hassanpouryouzband, A., Yang, J., & Tohidi, B. (2020). Heat transfer in unfrozen and frozen porous media: Experimental measurement and pore-scale modeling. *Water Resources Research*, *56*(9), e2020WR027885. https://doi.org/10.1029/2020WR027885

Wandel, A. P. (2023). Proof that all dissipation rates are only functions of time for transported joint-normal distributions. *Physics of Fluids*, *35*(4), 041703. https://doi.org/10.1063/5.0142876

Wang, B. (2021). Pore-scale modeling of fluid flow and particle transport in multi-scale porous media. LSU Doctoral Dissertations. https://digitalcommons.lsu.edu/gradschool_dissertations/5701

Yang, X., Mehmani, Y., Perkins, W. A., Pasquali, A., Schönherr, M., Kim, K., et al. (2016). Intercomparison of 3D pore-scale flow and solute transport simulation methods. *Advances in Water Resources*, *95*, 176–189. https://doi.org/10.1016/j.advwatres.2015.09.015

Zahasky, C., & Benson, S. M. (2022). Preferential solute transport in low permeability zones during spontaneous imbibition in heterogeneous porous media. *Water Resources Research*, *58*(1), e2020WR029460. https://doi.org/10.1029/2020wr029460

Zhang, C., Suekane, T., Minokawa, K., Hu, Y., & Patmonoaji, A. (2019). Solute transport in porous media studied by lattice Boltzmann simulations at pore scale and X-ray tomography experiments. *Physical Review E*, *100*(6), 063110. https://doi.org/10.1103/PhysRevE.100.063110

Zhang, X., Ma, F., Yin, S., Wallace, C. D., Soltanian, M. R., Dai, Z., et al. (2021). Application of upscaling methods for fluid flow and mass transport in multi-scale heterogeneous media: A critical review. *Applied Energy*, *303*, 117603. https://doi.org/10.1016/j.apenergy.2021.117603

Zhou, H., Yu, X., Chen, C., Lu, S., Wu, L., & Zeng, L. (2019). Pore-scale lattice Boltzmann modeling of solute transport in saturated biochar amended soil aggregates. *Journal of Hydrology*, *577*, 123933. https://doi.org/10.1016/j.jhydrol.2019.123933